American Mineralogist, Volume 91, pages 1006–1024, 2006

Microstructure and magnetism in the ilmenite-hematite solid solution: A Monte Carlo simulation study

RICHARD J. HARRISON*

Department of Earth Sciences, University of Cambridge, Downing Street, Cambridge CB2 3EQ, U.K.

ABSTRACT

The energetics of magnetic and cation ordering have been modeled using an atomistic approach based on empirical exchange interaction parameters. The model has been applied to the study of magnetic and cation ordering in the ilmenite-hematite solid solution via Monte Carlo simulations, providing new insight into the effect of nanoscale microstructures on the magnetic properties of this system. The lowest energy state for intermediate compositions is an intergrowth of cation-disordered antiferromagnetic (AF) hematite and cation-ordered paramagnetic (PM) ilmenite, separated by mixed Fe^{2+}/Fe^{3+} "contact layers." The intergrowth carries a stable defect moment ("lamellar magnetism") due to the presence of uncompensated spins. The net magnetization is parallel to the spin alignment direction, i.e., perpendicular to the spin-canted magnetization of the AF hematite. Contact-layer spins are coordinated to fewer magnetic neighbors than bulk spins and thus disorder more rapidly on heating. This leads to a decrease of net moment with increasing temperature. A small net moment is present, however, up to the Néel temperature of the AF hematite phase. The maximum temperature for acquisition of a chemical remanent magnetization due to lamellar magnetism is 800 ± 25 K, corresponding to the temperature for the eutectoid reaction PM hematite → AF hematite + PM ilmenite. If only cation interactions are considered, Fe^{3+} and Fe^{2+} in the contact layers become ordered so that Fe^{3+} shares an octahedral face with Fe^{3+} in the neighboring hematite layer and Fe^{2+} shares an octahedral face with Ti^{4+} in the neighboring ilmenite layer. If both cation and magnetic interactions are considered, however, an alternative ordering scheme is stabilized, whereby Fe^{3+} shares an octahedral face with Ti^{4+} in the neighboring ilmenite layer and Fe^{2+} shares an octahedral face with Fe^{3+} in the neighboring hematite layer.

The model has been used to investigate the nature of exchange coupling between ordered/antiordered domains and disordered antiphase boundaries, with a view to elucidating the mechanism of self-reversed thermoremanent magnetization. Antiphase boundaries are enriched in Fe relative to the ordered/antiordered domains, with enhanced enrichment observed in simulations performed within the PM hematite + PM ilmenite miscibility gap. Monte Carlo simulations of magnetic ordering show no evidence of self-reversal in systems containing two equally well-ordered ferrimagnetic (FM) domains separated by Fe-enriched AF boundaries. Systems displaying partial long-range order, however, do display self-reversed magnetization. Partial long-range order is characterized by a mixture of highly ordered Ti-rich FM domains and poorly ordered Fe-rich domains with a weak FM moment. The magnetic ordering temperature of the poorly ordered Fe-rich domains is significantly higher than that of the highly ordered Ti-rich domains, and act as the "*x*-phase." Evidence in support of the proposed mechanism from neutron diffraction and transmission electron microscopy is presented.

Keywords: Magnetism, microstructure, ilmenite, hematite

INTRODUCTION

The magnetic properties of the ilmenite-hematite solid solution are profoundly influenced by nanoscale microstructures associated with subsolvus exsolution and cation ordering. Slowly cooled rocks containing finely exsolved members of the hematite-ilmenite series have strong and extremely stable magnetic remanence, suggesting an explanation for some magnetic anomalies in the deep crust and on planetary bodies that no longer retain a magnetic field, such as Mars (McEnroe et al. 2001, 2002, 2004a–c; Kasama et al. 2004). This remanence has been attributed to a stable ferrimagnetic substructure originating from the coherent interface between nanoscale ilmenite and hematite exsolution lamellae (the so-called "lamellar magnetism hypothesis;" Harrison and Becker 2001; Robinson et al. 2002, 2004). Rapidly cooled members of the hematite-ilmenite series, on the other hand, are well known for their ability to acquire self-reversed thermoremanent magnetization. This phenomenon is related to the presence of fine-scale twin domains that form on cooling through the $R\bar{3}c$-$R\bar{3}$ cation ordering phase transition (Ishikawa and Syono 1963; Nord and Lawson 1989, 1992; Hoffman 1992; Bina et al. 1999; Prévot et al. 2001; Lagroix et al. 2005).

Lamellar magnetism and self-reversed thermoremanent magnetization are both consequences of the coupling between magnetic and cation ordering. This paper investigates the nature of this coupling through the development of an atomistic model

* E-mail: rjh40@esc.cam.ac.uk

0003-004X/06/0007–1006$05.00/DOI: 10.2138/am.2006.2008

of magnetic and cation ordering in ilmenite-hematite. The model accurately predicts the equilibrium degree of magnetic and cation order as a function of temperature and bulk composition, and reproduces the well-known topology of the equilibrium phase diagram. Monte Carlo methods are used to simulate nanoscale microstructures resulting from both slow cooling through the low-temperature miscibility gap and rapid cooling through the high-temperature cation order-disorder phase transition. The simulations are then used to investigate the nature of the coupling between magnetism and microstructure and the distribution of cations and spins throughout the heterogeneous system. The implications of the results to both lamellar magnetism and self-reversed thermoremanent magnetization are discussed in light of new experimental evidence from neutron diffraction and transmission electron microscopy.

THEORETICAL BACKGROUND

Crystal and magnetic structure

Hematite has the corundum structure with space group $R\bar{3}c$. The O anions are in distorted hexagonal close-packed arrangement, with Fe^{3+} occupying two-thirds of the octahedral sites to form symmetrically equivalent layers parallel to (001). Ilmenite adopts a related structure with Fe^{2+} and Ti^{4+} partitioned onto alternating A and B layers (Fig. 1). This partitioning destroys the equivalency of the layers, reducing the symmetry to $R\bar{3}$. The solid solution is formed via the substitution $2\,Fe^{3+} = Fe^{2+} + Ti^{4+}$. Fe^{3+} is distributed equally over the A and B layers. Fe^{2+} and Ti are ordered onto A and B layers at low temperatures, but become disordered over both layers at high temperatures, leading to a phase transition from $R\bar{3}$ to $R\bar{3}c$. The connectivity of the cation substructure is summarized in Table 1.

Hematite has a canted antiferromagnetic (CAF) structure with a Néel temperature of 675 °C. The antiparallel magnetic sublattices coincide with the A and B cation layers (Fig. 1). Between 675 and –10 °C (the Morin transition), the sublattice spins lie within the basal plane and are canted by a small angle about [001], producing a weak parasitic moment perpendicular to the direction of spin alignment. Below –10 °C, the spins lie parallel and antiparallel to [001] and the spin canting is lost. Ilmenite has an antiferromagnetic (AF) structure with spins parallel and antiparallel to [001] and a Néel temperature of around 60 K. The disordered solid solution is CAF with spins parallel to the basal plane. The ordered solid solution is ferrimagnetic (FM) because the concentration of Fe on the A and B layers is unequal (Ishikawa and Akimoto 1957; Ishikawa 1958, 1962; Ishikawa and Syono 1963; Harrison 2000). Spins are again parallel to the basal plane.

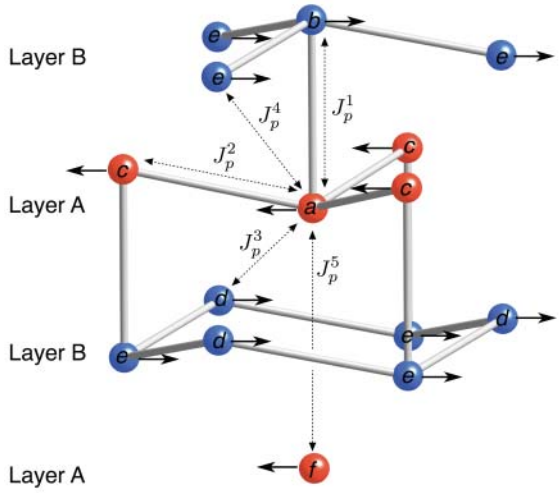

FIGURE 1. Definition of the chemical interaction types, J_p^q, for the first 5 coordination shells of the $R\bar{3}$ structure. Numerical values of J_p^q are given in Table 1 (after Harrison et al. 2000a). Cations are ordered onto alternating (001) layers A (red) and B (blue). The antiferromagnetic ordering of spins is indicated by the arrows.

Chemical energy model

The chemical energy of the solid solution is expressed in terms of chemical exchange interaction parameters, $J_{p,q}^{\text{chem}}$ (Bosenick et al. 2001):

$$E_{\text{chem}} = E_0 + \sum_{p,q} N_{p,q} J_{p,q}^{\text{chem}} \quad (1)$$

The interaction parameters describe the energy associated with placing a pair of unlike cations at a given separation within the structure. The labels p and q define the cation-cation pair and the cation-cation distance, respectively (see Table 1 for definitions). $N_{p,q}$ is the number of interactions per supercell for a given interaction type (counted using periodic boundary conditions). E_0 is constant for a fixed bulk composition, and can be neglected. Positive values of $J_{p,q}^{\text{chem}}$ mean that unlike cation-cation neighbors are energetically unfavorable, thus creating a driving force for exsolution. Negative values of $J_{p,q}^{\text{chem}}$ mean that unlike cation-cation neighbors are energetically favorable, thus creating a driving force for cation ordering.

Several strategies exist for determining numerical values for the chemical interaction parameters. In some cases, e.g., aluminosilicates, values can be determined empirically by combining NMR and calorimetric data (Phillips et al. 1992). However, this approach is limited to nearest-neighbor interactions only. Using ab initio or static lattice calculations, it is possible to calculate E_{chem} for several different cation configurations and then use Equation 1 to extract values for $J_{p,q}^{\text{chem}}$ (Becker et al. 2000; Warren et al. 2000a, 2000b; Dove 2001; Bosenick et al. 2001; Vinograd et al. 2004). This approach can provide valuable physical insight into the magnitude and sign of the interaction parameters, even for distant neighbors, and can highlight unexpected relationships between the interaction parameters and local structure (Bosenick et al. 2000). When many well-constrained experimental observations are available, and the aim is to produce a model that reproduces these observations as closely as possible, a combined computational/empirical approach can be employed. Computations are used to determine physically reasonable estimates for the magnitude and sign of the dominant interaction parameters. These values are then refined by comparing the predictions of the model to the experimental data. The potential risk is that the link between interaction parameters and local structure is lost or cannot be established unambiguously. This risk can be assessed by testing the predictions of the model against experimental observations that were not used as constraints in the fitting procedure.

Harrison et al. (2000a) used a combined computational/empirical approach to derive a set of chemical exchange interac-

TABLE 1. Summary of cation-cation interaction types and their chemical and magnetic interaction parameters

Interaction type (q)	Cation pair (see Fig. 1 for definitions)	Cation-cation distance (Å)	Number of interactions per cation	Inter/intra/double layer interaction	Octahedral sharing	Cation-oxygen-cation bond angle (°)	Chemical interaction parameter (K) p = 1 = Fe^{2+}-Ti p = 2 = Fe^{3+}-Ti p = 3 = Fe^{2+}-Fe^{3+}			Magnetic interaction parameter (K) p = 1 = Fe^{3+}-Fe^{3+} p = 2 = Fe^{2+}-Fe^{2+} p = 3 = Fe^{2+}-Fe^{3+}		
							$J^{chem}_{1,q}$	$J^{chem}_{2,q}$	$J^{chem}_{3,q}$	$J^{mag}_{1,q}$	$J^{mag}_{2,q}$	$J^{mag}_{3,q}$
1	a–b	2.9	1	Interlayer	Face	86.5	–2418	–554	–483	10.2	2.55	6.375
2	a–c	2.971	3	Intralayer	Edge	93.9	–1683	420	–337	2.72	0.68	1.7
3	a–d	3.36	3	Interlayer	Corner	119.7	–957	–322	–191	–50.49	–12.62	–31.55
4	a–e	3.71	6	Interlayer	Corner	131.6	–957	–322	–191	–39.44	–9.86	–24.65
5	a–f	3.99	1	Double	None	N.A.	0	0	0	–1.7	–0.425	–1.06

tion parameters for ilmenite-hematite (Table 1).[1] The signs and relative magnitudes of the parameters were determined using a combination of static lattice calculations and crystal-chemical principles (Burton and Kikuchi 1984). The magnitudes of the parameters were then refined by fitting to neutron diffraction data for the $R\bar{3}$ to $R\bar{3}c$ phase transition in samples with x = 0.7, 0.8, 0.9, and 1.0 (Harrison et al. 2000b). The validity of the parameters can be tested by comparing the predicted degree of cation order for x = 0.6 with the subsequent neutron diffraction data of Harrison and Redfern (2001). Excellent agreement between predicted and observed behavior is found (Fig. 2). Nevertheless, independent confirmation of the parameters used via ab initio calculations would be desirable.

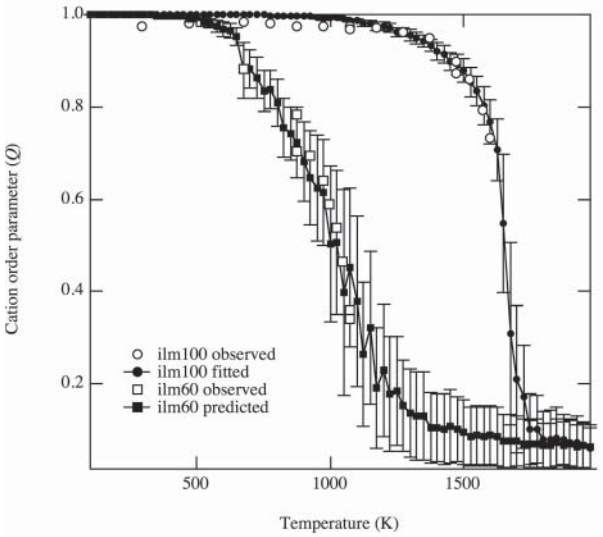

FIGURE 2. Comparison of observed and simulated degree of cation order in Ilm_{60} (squares) and Ilm_{100} (circles). Open symbols show the variation in Q vs. T determined via neutron diffraction (Harrison et al. 2000b; Harrison and Redfern 2001). Closed symbols show the results of Monte Carlo simulations with a 4 × 4 × 8 supercell (this study).

Magnetic energy model

To extend the model of Harrison et al. (2000a), we now take account of the magnetic contribution to the energy of the solid solution. Because we are primarily concerned with the development of an energy model suitable for thermodynamic modeling, no account of the difference in magnetocrystalline anisotropy between hematite and ilmenite is made, and magnetic moments are constrained to lie within the basal plane across the entire solid solution. This does not affect the thermodynamic properties significantly, but will lead inevitably to an inability to predict correctly the magnetic structure of ilmenite-rich compositions at low temperature, where competing exchange interactions and magnetocrystalline anisotropy lead to spin-glass behavior (Ishikawa et al. 1985; Arai et al. 1985a, 1985b; Arai and Ishikawa 1985). Similarly, because the interactions causing spin canting are around a factor of 1000 smaller than the superexchange interactions causing antiferromagnetic ordering (Morrish 1994), canting of spins will be neglected.

The magnetic moment, M, of an Fe^{3+} or Fe^{2+} cation is (assuming spin-only contributions):

$$M = gM_S\mu_B \tag{2}$$

where g is the Landé factor (g = 2 for pure spin moments), μ_B is the Bohr magneton ($\mu_B = 9.274 \times 10^{-24}$ Am^2), and M_S is the component of spin, S, parallel to the basal plane. Fe^{3+} and Fe^{2+} cations contain 5 and 4 unpaired electrons in their 3d orbitals, respectively, yielding S = 5/2 for Fe^{3+} and S = 4/2 for Fe^{2+}. M_S can adopt (2S + 1) values from –S to S. The magnetic contribution to the energy is calculated in terms of magnetic superexchange interaction parameters, $J^{mag}_{p,q}$:

$$E_{mag} = -J^{mag}_{p,q}\sum_{\langle i,j\rangle}\vec{S}_i\cdot\vec{S}_j \tag{3}$$

$$= -J^{mag}_{p,q}\sum_{\langle i,j\rangle}M^i_S M^j_S \tag{4}$$

where the sum is made over all neighboring atoms i and j, assuming periodic boundary conditions. Values for the magnetic interaction parameters for Fe^{3+}-Fe^{3+} superexchange in hematite and Fe^{2+}-Fe^{2+} superexchange in ilmenite are obtainable from inelastic neutron-scattering experiments (Samuelsen 1969; Samuelsen and Shirane 1970). Due to the cation-ordered nature of pure ilmenite, these experiments cannot yield values for Fe^{2+}-Fe^{2+} interlayer interactions. Similarly, no data are available for Fe^{2+}-Fe^{3+} interactions. Values for these missing magnetic interaction parameters have been estimated from the available data for Fe^{3+}-Fe^{3+} interactions in hematite, and then refined by comparing the predictions of the model to the observed variation in Néel temperature vs. composition in the solid solution. The resulting interaction parameters are listed in Table 1. The fitting procedure is described in the results section. Note that the first- and second-nearest-neighbor magnetic interactions are weak due to the ~90° cation-oxygen-cation bond angle for face- and edge-sharing octahedra, which is an unfavorable configuration

[1]Note that the parameters used here are a factor of two smaller than those reported by Harrison et al. (2000a) due to a difference in the Monte Carlo simulation code used.

for superexchange (Harrison and Becker 2001). The dominant magnetic interactions are the third- and fourth-nearest-neighbor interlayer interactions, which correspond to corner-sharing octahedra with larger cation-oxygen-cation bond angles.

SIMULATION METHODS

The starting point for the Monte Carlo simulations is a supercell of cation positions, arranged with the topology and connectivity of the ilmenite-hematite structure. Two supercells were generated for this study: a $4 \times 4 \times 8$ supercell containing 1536 cation positions and an $8 \times 8 \times 8$ supercell containing 6144 cation positions. Each cation position is occupied by either an Fe^{2+}, an Fe^{3+}, or a Ti^{4+} cation. The numbers of each cation are determined by the bulk composition, $Fe_t^{2+}Ti_x^{4+}Fe_{2-2x}^{3+}O_3$, and kept fixed during the simulation. The starting cation configuration can be either ordered, whereby Fe^{2+} and Ti^{4+} are partitioned completely onto alternating A and B layers, or disordered, whereby all three cations are distributed randomly. Once the cation configuration has been chosen, each Fe^{2+} and Fe^{3+} cation is assigned an appropriate value of M_S. All simulations are initialized with a fully ordered spin configuration, such that Fe^{2+} and Fe^{3+} on the A layers are assigned $M_S = +4/2$ and $+5/2$, respectively, while those on the B layers are assigned $M_S = -4/2$ and $-5/2$. This leads to an antiferromagnetic starting structure for systems with disordered cation configurations and a ferrimagnetic starting structure for systems with ordered cation configurations.

The total energy of the solid solution, E, is the sum of chemical and magnetic contributions. At equilibrium, each configuration of the supercell occurs with a thermodynamic probability determined by the temperature, T, and the Boltzmann distribution, $\exp(-E/T)$, where both E and T are measured in Kelvin (Table 1). In a Monte Carlo simulation, the equilibrium thermodynamic properties are determined by averaging over several configurations generated with their correct thermodynamic probability. The supercell is generated with an arbitrary starting configuration. Pairs of atoms are chosen at random and their positions are swapped. If the change in energy, ΔE, due to the swap is negative, then the swap is accepted. If ΔE is positive, then the swap is accepted with a probability $\exp(-\Delta E/T)$. After a sufficient number of swaps the system reaches equilibrium, with configurations generated independently of the starting configuration. The equilibrium properties (energy, degree of cation, magnetic order, etc.) can then be determined by averaging over several steps until the desired statistical significance is reached.

For systems displaying coupled magnetic and cation ordering, we define three distinct types of types of Monte Carlo step. The first is a referred to as a "pure chemical" step. Two cations are chosen at random and their positions swapped. If either of the chosen cations is magnetic, then the swap will also change the configuration of spins. However, only the chemical contribution to the energy change, ΔE_{chem}, is used to determine whether the swap is accepted or rejected. Repeating steps of this type allow the system to attain its equilibrium degree of cation order—based on the chemical interaction parameters alone—but has the side effect of randomizing the magnetic spin configuration over time. The second is referred to as a "pure magnetic" step. A single magnetic cation is chosen at random and its spin variable, M_S, is changed to one of $(2S+1)$ values between $-S$ and $+S$ at random. Only the magnetic contribution to the energy, ΔE_{mag}, is used to determine whether the change is accepted or rejected. Repeating steps of this type allows the system to attain its equilibrium degree of magnetic order—based on the magnetic interaction parameters alone—while leaving the cation distribution unchanged. The third is referred to as a "combined cation" step, which is similar to a pure cation step, except that the total energy change, $\Delta E = \Delta E_{chem} + \Delta E_{mag}$, is used to determine whether the swap is accepted or rejected.

On this basis, we define three different classes of simulation. A "cation only" simulation involves only pure cation steps, and is used to study the equilibrium degree of cation order independently of magnetic interactions. A "magnetic only" simulation involves only pure magnetic steps, and is used to study the equilibrium degree of magnetic order for a fixed distribution of cations. A "combined" simulation involves performing a relatively small number of combined cation steps (typically of the order of 1000) following by an equal number of pure magnetic steps. This alternating sequence is then repeated until the system acquires its equilibrium degree of cation and magnetic order. The alternation of cation swaps and spin flips is necessary to allow the spin values of the magnetic cations to deviate from their original starting value (spins are conserved during cation swaps). By using the total energy change to determine whether or not a swap is accepted, we ensure that the magnetic and cation ordering processes behave as a single coupled process, rather than two independent ordering processes.

The degree of long-range cation order, Q, is defined as:

$$Q = \frac{N_{Ti}^{B} - N_{Ti}^{A}}{N_{Ti}^{A} + N_{Ti}^{B}} \quad (5)$$

where N_{Ti}^{A} and N_{Ti}^{B} are the number of Ti^{4+} cations on A and B layers, respectively. Q varies from 0 in the disordered state (with Ti equally distributed over A and B layers) to ±1 in the ordered/antiordered state (with Ti fully partitioned onto either the B or A layers, respectively). The degree of long-range magnetic order is defined as the average sum of spins on the A and B sublattices:

$$S_A = \frac{1}{N_A} \sum M_S^A \quad (6)$$

$$S_B = \frac{1}{N_A} \sum M_S^B \quad (7)$$

where N_A and N_B are the total number of cation positions on the A and B sublattice, respectively. The net magnetization per formula unit then follows from Equation 2:

$$M_{net} = 2(|S_A| - |S_B|)\mu_B \quad (8)$$

Simulations are run for a total of 5 million steps for the $4 \times 4 \times 8$ supercell and 20 million steps for the $8 \times 8 \times 8$ supercell, with a pre-equilibration run of 10^5 steps in each case. The cation and magnetic order parameters are calculated after every 1000 steps. The variation in energy and degree of magnetic and cation order are monitored graphically throughout the simulation to ensure that the system has converged to an equilibrium state before averaging. Results are presented as the average values of Q, $|S_A|$, and $|S_B|$, together with their standard deviations. At the end of each simulation, a snapshot of the final cation/spin configuration is recorded. When the standard deviation is low (i.e., at low temperatures), such snapshots are a good representation of the average equilibrium state. When the standard deviation is high, however, the snapshot may deviate significantly from the average equilibrium state.

RESULTS

Magnetic ordering in end-member hematite

Figure 3 compares the simulated temperature dependence of sublattice spin in pure Fe_2O_3 with the mean-field solution for

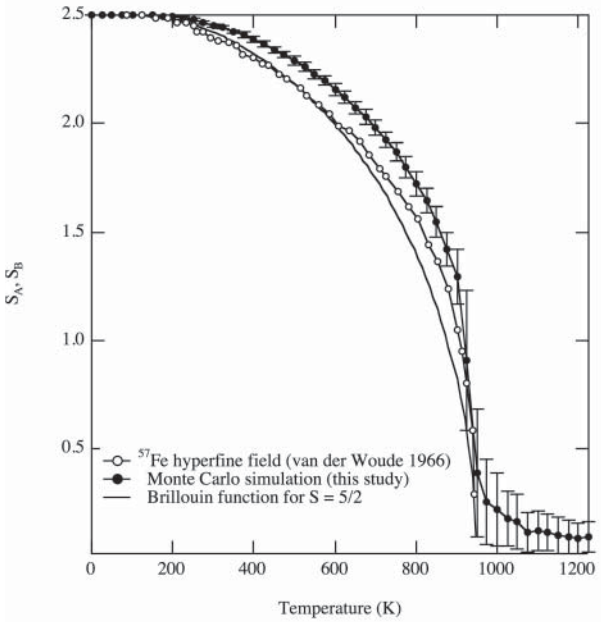

FIGURE 3. Comparison of observed, theoretical, and simulated sublattice spin vs. temperature in pure Fe_2O_3. Open circles show the observed variation in sublattice spin determined using Mössbauer spectroscopy (van der Woude 1966). Solid curve shows the Brillouin function for an $S = 5/2$ cation (i.e., Fe^{3+}). Closed circles show the results of the Monte Carlo simulations using a $4 \times 4 \times 8$ supercell and the magnetic interaction parameters listed in Table 1. The tail at $T > T_N$ is an artifact caused by the finite size of the supercell.

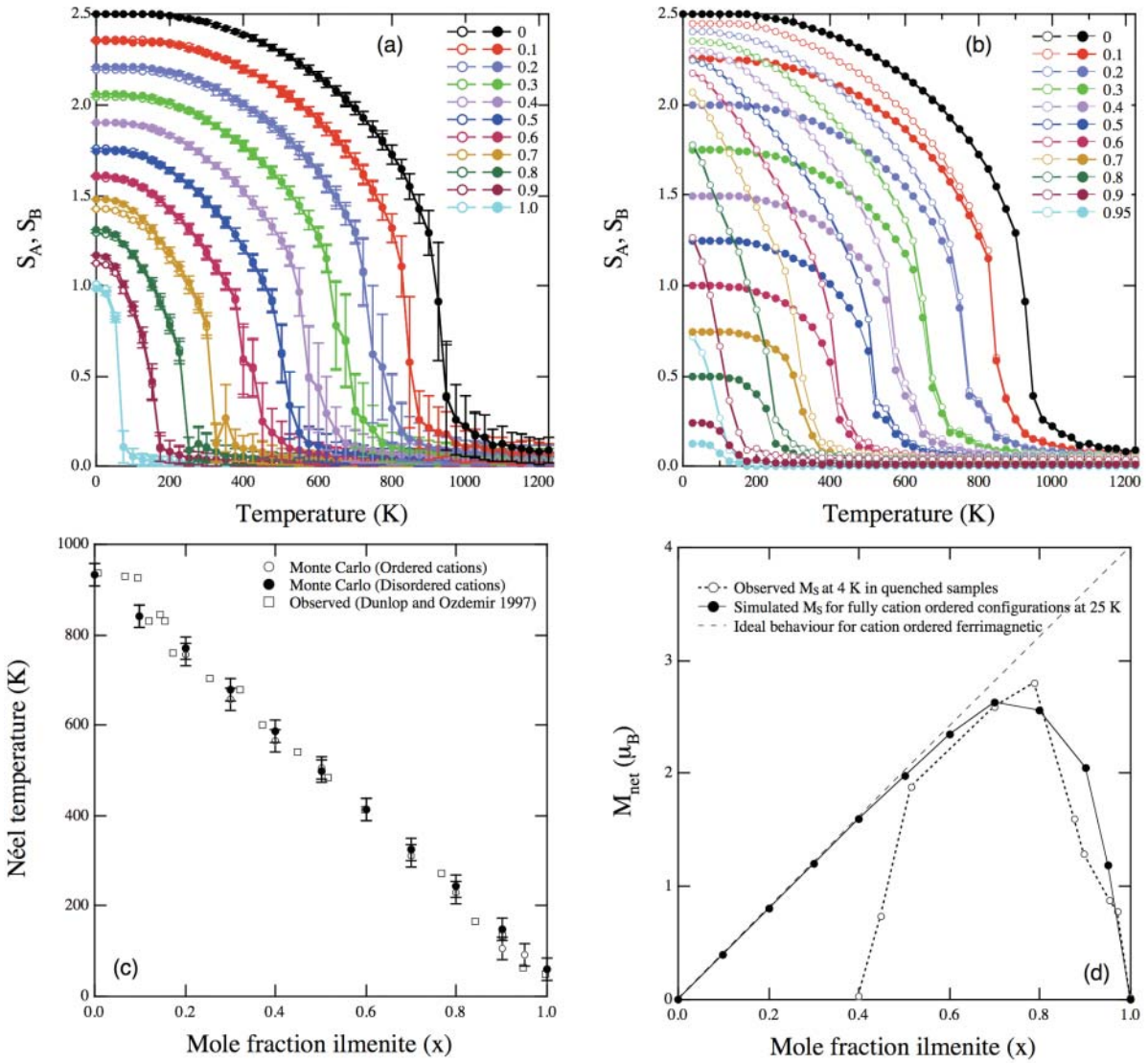

FIGURE 4. "Magnetic only" simulation of sublattice spins S_A and S_B vs. temperature and bulk composition (x) for supercells with (**a**) fully disordered and (**b**) fully ordered cation configurations. (**c**) Comparison of calculated Néel temperatures for ordered and disordered cation configurations (open and closed circles, respectively). Experimental results (open squares) were taken from Dunlop and Özdemir (1997). (**d**) Comparison of net magnetization (Eq. 8) at 25 K for the ordered cation configurations (closed circles) and observed values of saturation magnetization determined at 4 K (open circles; Ishikawa and Akimoto 1957; Ishikawa 1962, 1964). Ideal variation in net magnetization is indicated by the dashed line.

$S = 5/2$ and the ^{57}Fe hyperfine field measured using Mössbauer spectroscopy (van der Woude 1966; Morrish 1994). Simulations performed with the raw exchange constants of Samuelsen and Shirane (1970) produced a Néel temperature, T_N, significantly higher than the experimental value of 948 K. A similar observation was made by Burton and Kikuchi (1984), who used the same exchange constants in a cluster variation method (CVM) calculation of magnetic ordering in hematite. Improved agreement between simulated and observed T_N was obtained by multiplying the raw exchange constants by 0.85 (Table 1). The tail in the simulated sublattice spin at $T > T_N$ is an artifact caused by the finite size of the supercell (Mouritsen 1984). For convenience, we define T_N as the point of inflection in the magnetization curve.

Magnetic ordering in the solid solution

The effect of substituting Ti into the hematite structure was investigated by performing "magnetic only" simulations of supercells with fully disordered and fully ordered cation configurations. Fully disordered configurations show antiferromagnetic ordering with $|S_A| = |S_B|$ (Fig. 4a). Fully ordered configurations show ferrimagnetic ordering with $|S_A| > |S_B|$ (Fig. 4b). T_N is equal in both cases. This result contrasts with the experimental observation that T_N is higher for the cation-ordered solid solution than for the cation-disordered solid solution (Ishikawa 1962). This discrepancy may be explained by a small difference in the stoichiometry of samples that have been quenched from high temperature and those that have been annealed at lower

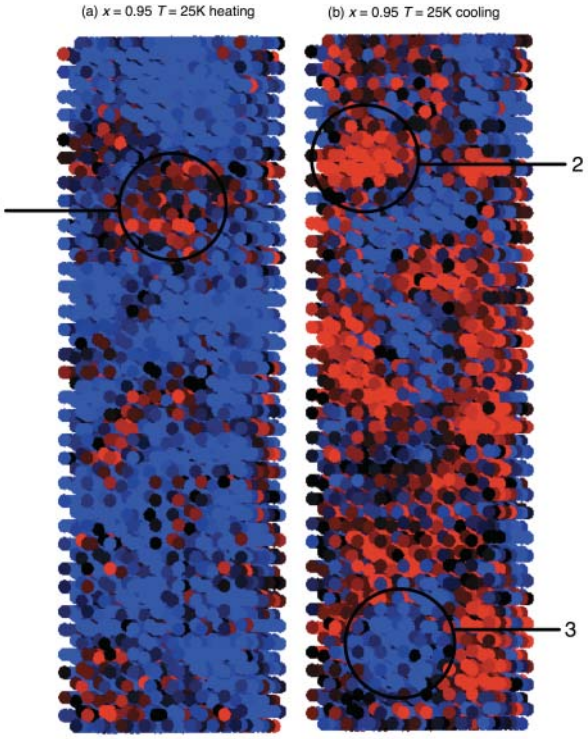

FIGURE 5. Snapshots of "magnetic only" simulations performed on an 8 × 8 × 8 supercell with a fully ordered cation configuration and bulk composition $x = 0.95$. Each circle represents the local ferrimagnetic moment at a given cation site within the supercell, calculated by averaging the spin values within the first 4 coordination shells around each site (blue = positive, red = negative). The brightness of the color is proportional to the magnitude of the net ferrimagnetic moment. (**a**) Simulation performed at 25 K with a starting configuration of fully ordered ferrimagnetic spins. Long-range ferrimagnetic order was maintained throughout the simulation. Enhanced spin disorder (e.g., region 1) occurs in regions devoid of Fe^{3+} cations in the Ti layer. (**b**) Simulation performed at 25 K with a starting configuration of fully disordered spins. Short-range ferrimagnetic order is maintained throughout the simulation. Regions 2 and 3 have opposing net ferrimagnetic moments, indicated by the red and blue colors.

temperatures. Large variations in T_N with small changes in high-temperature non-stoichiometry are well documented, for example, in the titanomagnetite system (Hauptman 1974). The calculated T_N decreases linearly with increasing mole fraction ilmenite (Fig. 4c). The decrease is caused by a combination of the dilution effect (i.e., a reduction in the probability of exchange interaction due to the presence of non-magnetic cations) and an interaction weakening effect (i.e., a reduction in the average strength of exchange interactions due to the replacement of Fe^{3+} by Fe^{2+}). Initial simulations were performed by assuming exchange constants for Fe^{2+}-Fe^{2+} and Fe^{2+}-Fe^{3+} interactions equal to those for Fe^{3+}-Fe^{3+} interactions in hematite. This assumption leads to a significant underestimation of the slope of the T_N-x line (Harrison and Becker 2001), suggesting that exchange constants for Fe^{2+}-Fe^{2+} and Fe^{2+}-Fe^{3+} interactions are much weaker than those for Fe^{3+}-Fe^{3+} interactions. To reproduce the observed slope of the T_N-x line (Fig. 4c) it was necessary to reduce the strength of the Fe^{2+}-Fe^{2+} interactions to 1/4 of the strength of the Fe^{3+}-Fe^{3+} interactions. The Fe^{2+}-Fe^{3+} exchange constants were set to the average of those for Fe^{2+}-Fe^{2+} and Fe^{3+}-Fe^{3+} interactions. Weakening of the Fe^{2+}-Fe^{2+} interactions is expected due to the slightly larger Fe^{2+}-O distance. However, independent confirmation of the magnitude of this weakening via ab initio calculations would be desirable. It is worth noting that the Néel temperatures of natural hematites contained within nanoscale intergrowths often lie significantly above the T_N-x line in Figure 4c (McEnroe et al. 2004a). The reason for this observation is not yet clear, but may be related to the presence of lattice strain at the coherent interface between hematite and ilmenite.

The ferrimagnetic moment of the cation-ordered solid solution is compared with the ideal moment in Figure 4d. The fully ordered cation configuration can be written:

$$\left(Fe_x^{2+}Fe_{1-x}^{3+}\right)_A\left(Ti_x^{4+}Fe_{1-x}^{3+}\right)_B O_3 \quad (9)$$

Assuming perfect ferromagnetic alignment of spins on the A and B sublattices, and perfect antiparallel alignment of the A sublattice relative to the B sublattice, the ideal ferrimagnetic moment per formula unit is $4x\mu_B$ (dashed line in Fig. 4d). Ideal values are observed for $x \leq 0.5$ (Fig. 4d). Negative deviations from ideality are observed for $x > 0.5$, with rapid loss of the ferrimagnetic moment occurring between $0.8 < x < 1$. This loss coincides with the breakdown of long-range magnetic order on the Fe-rich sublattice, caused by dilution of Fe on the neighboring Ti-rich sublattices. Dilution results in an increasing number of Fe cations that are completely surrounded by Ti on the adjacent sublattices. The alignment of spins in such regions is determined solely by the weak ferromagnetic intralayer interactions ($J_{p,2}^{mag}$; Table 1), leading to an increase in local magnetic disorder. An example of this phenomenon is shown in Figure 5a. The majority of the supercell is magnetically ordered with a large positive ferrimagnetic moment (blue circles). Region 1, which is centered on an Fe cation surrounded by Ti, has relatively disordered spins and a small negative ferrimagnetic moment (dark red circles). Perfect ferromagnetic order is maintained on the Ti-rich sublattice at all compositions, as the alignment of these spins is determined by strong antiferromagnetic exchange with Fe on the neighboring sublattices ($J_{p,3}^{mag}$ and $J_{p,4}^{mag}$; Table 1).

The loss of ferrimagnetic moment over the composition range $0.8 < x < 1$ agrees very well with experimental observations of saturation magnetization at 4 K (open circles in Fig. 4d; Ishikawa and Akimoto 1957; Ishikawa 1962, 1964). This compositional range is known to exhibit spin-glass behavior at low temperature (Ishikawa et al. 1985; Arai et al. 1985a, 1985b; Arai and Ishikawa 1985). Due to the simplifications made in the current model (e.g., ignoring the different magnetocrystalline anisotropies of Fe^{3+} and Fe^{2+}), we cannot hope to reproduce the spin configurations that are observed in the spin glass using neutron diffraction (Arai et al. 1985a, 1985b; Arai and Ishikawa 1985). Nevertheless, the model does reproduce certain key features of the spin glass. The failure to achieve long-range magnetic order in the spin-glass region has been attributed to the generation of isolated ferrimagnetic clusters (Ishikawa et al. 1985). These clusters display superparamagnetic behavior below T_N, and become frozen into a spin glass state at lower temperature due to the onset of ilmenite-like antiferromagnetic ordering across two cation layers. Long-range magnetic order cannot be achieved due to

the frustration of spins at the edges of the ferrimagnetic clusters. This model was investigated by cooling an $8 \times 8 \times 8$ supercell with $x = 0.95$ from above T_N to 25 K (Fig. 5b). In contrast to the simulation performed at 25 K with a fully ordered starting spin configuration (Fig. 5a), the simulation performed on cooling did not develop long-range ferrimagnetic order. Instead, the supercell developed a high degree of short-range order, characterized by the presence of ferrimagnetic clusters with opposing net magnetizations (blue and red circles in Fig. 5b; e.g., regions 2 and 3). This finding provides some support for Ishikawa's theory of the origin of spin-glass behavior in this system.

Antiferromagnetic ordering in pure, cation-ordered ilmenite was found only below 4 K in the simulations, well below the observed Néel temperature of 55–60 K. This failure of the model indicates a significant underestimation of the Fe^{2+}-Fe^{2+} double layer interaction ($J^{mag}_{p,5}$; Table 1). Pure ilmenite with a disordered cation configuration developed antiferromagnetic order at $T_N = 60$ K (Fig. 4a). There is clearly a need for refinement of the exchange constants for ilmenite-rich members of the solid solution before the current model can be used to provide new insight into the behavior of the spin glass.

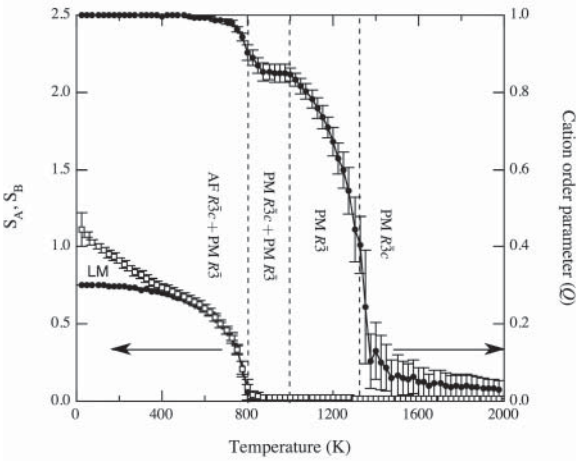

FIGURE 6. "Combined" simulation of simultaneous cation and magnetic ordering in ilm70 ($8 \times 8 \times 8$ supercell). Sublattice spins, S_A and S_B, are indicated by the open and closed squares, respectively (left axis). Cation order parameter, Q, is indicated by the closed circles (right axis). Dashed lines indicate the positions of the phase boundaries shown in Figure 8.

Coupled cation and magnetic ordering in the solid solution

Figure 6 illustrates the variation in S_A, S_B, and Q vs. T for a bulk composition $x = 0.7$ ($8 \times 8 \times 8$ supercell). The ordering curves define the boundaries between different regions of the equilibrium phase diagram. Above ~1300 K, the system is both chemically and magnetically disordered (PM $R\bar{3}c$, where PM stands for paramagnetic). Below ~1300 K, the system is chemically ordered and magnetically disordered (PM $R\bar{3}$). The non-zero value of Q within the PM $R\bar{3}c$ stability field is an artifact caused by the finite size of the supercell. This tail is more pronounced in simulations using the smaller $4 \times 4 \times 8$ supercell, making it difficult to define a precise value for the $R\bar{3}c$ to $R\bar{3}$ transition temperature, T_c. For convenience we define T_c as the point of inflection in cation ordering curve.

At 1000 K there is a distinct kink in the cation ordering curve and the order parameter saturates temporarily at $Q = 0.85$. The same behavior has been observed experimentally using neutron diffraction (Harrison et al. 2000b). Experiments on a quenched sample with $x = 0.7$ showed Q reaching a maximum value of 0.85 in the temperature range 673–973 K. This was much lower than the value obtained by extrapolating the high-temperature equilibrium data, yet could not be explained as a failure of the sample to reach equilibrium. Harrison et al. (2000b) concluded that the observations were consistent with fine-scale chemical segregation. This conclusion is supported by the Monte Carlo simulations. Simulation snapshots below 1000 K reveal the supercell to be an intergrowth of two paramagnetic phases: an Fe-rich PM $R\bar{3}c$ phase and a Ti-rich PM $R\bar{3}$ phase. The degree of cation order in the PM $R\bar{3}$ phase increases on cooling, as expected. This is balanced, however, by the decrease in the amount of PM $R\bar{3}$ phase present as the PM $R\bar{3}c$ phase exsolves. At some lower temperature, the rate of increase in Q within the PM $R\bar{3}$ phase outweighs the rate of its decreasing phase fraction, and the average value of Q increases again.

The magnetic ordering transition PM $R\bar{3}c \rightarrow$ AF $R\bar{3}c$ occurs at 800 K. The PM $R\bar{3}$ phase remains paramagnetic at all temperatures. The most striking feature of the AF $R\bar{3}c$ + PM $R\bar{3}$ stability field is the large difference between $|S_A|$ and $|S_B|$ below 500 K. This difference cannot be explained in terms of the bulk properties of the two phases present; a bulk AF $R\bar{3}c$ phase has $|S_A| = |S_B|$; a bulk PM $R\bar{3}$ phase has $|S_A| = |S_B| = 0$. The maximum difference between $|S_A|$ and $|S_B|$ is 0.37 at 25 K, corresponding to a net ferrimagnetic moment of 0.74 μ_B per formula unit (Eq. 8). This is nearly one third of the maximum ferrimagnetic moment of a fully ordered single-phase solid solution with $x = 0.7$ (Fig. 4d), and is equivalent to the ferrimagnetic moment of a partially cation-ordered single-phase solid solution with $x = 0.7$ and $Q = 0.47$. This ferrimagnetism has been termed "lamellar magnetism." Its origin will be discussed in detail later.

Figure 7 summarizes the results of all simulations performed with the $4 \times 4 \times 8$ supercell. Simulations were performed over a grid of points in temperature-composition space, covering $100 \le T \le 1975$ K and $0 \le x \le 1$ in steps of $\Delta T = 25$ K and $\Delta x = 0.05$. The raw values of Q and S_B have been interpolated bilinearly with a sampling factor of 4 and displayed as color image plots in Figures 7a and 7b, respectively. T_c and T_N are defined by the green bands, which correspond to the points of inflection in the Q-T and S_B-T curves. These critical temperatures are used to track the phase boundaries identified in Figure 6 through temperature-composition space. The only phase boundary that is not clearly defined by T_c and T_N is the ilmenite-rich limb of the PM $R\bar{3}c$ + PM $R\bar{3}$ miscibility gap. The temperature of this boundary, T_E, was determined from the kink in the Q-T curves (Fig. 6) and verified by manually inspecting the supercell snapshots for evidence of phase separation. For this purpose it was necessary to use simulations performed with the 8× 8× 8 supercell, which were significantly less noisy than those performed with the $4 \times 4 \times 8$ supercell.

Numerical values of T_c, T_N, and T_E are listed in Table 2 and summarized in Figure 8. The key features are: (1) a pure magnetic ordering transition (PM $R\bar{3}c \rightarrow$ AF $R\bar{3}c$) in hematite-rich compositions; (2) a pure cation ordering transition (PM $R\bar{3}c \rightarrow$ PM $R\bar{3}$) in ilmenite-rich compositions; (3) a tricritical point at $x = 0.58 \pm 0.02$, $T = 1050 \pm 25$ K, corresponding to the top of the PM $R\bar{3}c$ + PM $R\bar{3}$ miscibility gap; and (4) a tricritical point at $x = 0.18 \pm 0.02$, $T = 800 \pm 25$ K, corresponding to the eutectoid reaction PM $R\bar{3}c \rightarrow$ AF $R\bar{3}c$ + PM $R\bar{3}$. It is useful to compare the positions of the two tricritical points with

previous predictions based on cluster variation methods ($x = 0.5$, $T = 948$ K and $x = 0.28$, $T = 793$ K; Burton and Davidson 1988) and macroscopic thermodynamic modeling ($x = 0.57$, $T = 1050$ K and $x = 0.3$, $T = 650$ K; Ghiorso 1997). Considering that no information about the position—or, indeed, the presence—of the PM $R\bar{3}c$ + PM $R\bar{3}$ miscibility gap was used in the derivation of the chemical interaction parameters, there is remarkable agreement between the predicted position of the first tricritical point and that of Ghiorso (1997), whose calibration did include experimental constraints on the position of the miscibility gap. The predicted position of the eutectoid point is in good agreement with that of Burton and Davidson (1988). The agreement improves when you consider that the eutectoid composition predicted by Burton and Davidson (1988) is likely to be significantly overestimated due to his underestimation of the slope of the T_N-x line. It is not clear why the eutectoid reaction predicted here and by Burton and Davidson (1988) is so different from that of Ghiorso (1997). Given that both Monte Carlo and cluster variation methods take proper account on short-range cation and magnetic order, an eutectoid temperature closer to 800 than 650 K seems the more likely.

In theory, the eutectoid reaction at 800 K should mark the onset of magnetic ordering for all bulk compositions between $x = 0.18$ (the eutectoid point) and $x = 0.82$ (the intersection of the eutectoid temperature with the ilmenite-rich limb of the PM $R\bar{3}c$ + PM $R\bar{3}$ miscibility gap). The expected behavior is observed, within error, for $x \leq 0.7$. Deviations from the expected behavior are observed for $x > 0.7$, with magnetic ordering occurring at a temperature significantly below 800 K. This effect is an artifact caused by the small size of hematite-rich precipitates in the two-phase intergrowth for bulk compositions close to the ilmenite-rich limb of the miscibility gap. The effective supercell size of an exsolved phase is much smaller than the size of the whole supercell, causing a significant underestimation of the Néel temperature.

Lamellar magnetism in the AF $R\bar{3}c$ + PM $R\bar{3}$ stability field

The origin of lamellar magnetism can be determined by examining snapshots of the cation/spin distribution for simulations performed within the AF $R\bar{3}c$ + PM $R\bar{3}$ stability field (Fig. 9). The supercell contains two precipitates of pure AF hematite within a host of pure PM ilmenite. The lower precipitate has a well-defined lamellar morphology with an atomically flat interface between it and the ilmenite host. It is 2 nm (~1.5 unit cells) thick, corresponding to the lower size limit of exsolution lamellae typically observed in natural samples (Robinson et al. 2002). The precipitate contains a total of 11 Fe-bearing cation layers: 9 Fe^{3+} layers bounded on either side by mixed Fe^{3+}-Fe^{2+} "contact" layers. The contact layers are followed by the Ti layers of the ilmenite host, whereafter the alternating sequence of Fe^{2+} and Ti^{4+} layers is established. This characteristic sequence of cation layers appears consistently throughout the AF $R\bar{3}c$ + PM $R\bar{3}$ stability field, and represents the lowest energy state of the exsolved system.

To form a hematite precipitate from an ordered ilmenite host we must start by substituting one Fe^{2+} layer and one Ti^{4+} layer by 2 Fe^{3+} layers. Growth of the hematite precipitate proceeds by the addition of Fe^{3+} layers in multiples of 2. Hence, without the formation of contact layers, each hematite precipitate would contain $2N$ Fe^{3+} layers (i.e., an even number). However, such a precipitate would be bounded by a Ti^{4+} layer on one side and an Fe^{2+} layer on the other side, making a total of $2N+1$ (i.e., an odd number) of Fe-bearing layers linked by strong negative superexchange interactions. No matter what the value of N, such a precipitate would be antiferromagnetic with one layer of uncompensated spins, yielding a net magnetic moment equivalent to the magnetic moment of the Fe^{2+} layer. The chemical and magnetic energy of the interfaces is lowered significantly if half the cations in one Fe^{3+} layer are exchanged with half the cations in the Fe^{2+} layer to form two contact layers. This rearrangement of cations does not change the net magnetic moment, however, which remains equal to the magnetic moment of one Fe^{2+} layer (Robinson et al. 2004). Lamellar magnetism can be considered as a type of defect moment that arises as a consequence of the natural tendency for nanoscale hematite lamellae to form with an odd number of Fe-bearing layers; irrespective of the specific chemical composition and internal structure of the contact layers predicted by the Monte Carlo model, there is always one layer of uncompensated spins—and a corresponding magnetic moment—associated with each precipitate (Fig. 9c).

The upper precipitate has a less well-defined shape and an atomically rough interface with the ilmenite host. It is 0.7–1.4 nm (~0.5–1 unit cells) thick, corresponding to the length scale of the compositional clustering commonly observed in natural samples in the vicinity of precipitate-free zones (McEnroe et al. 2002). The more irregular shape and rough interface of the upper precipitate enhances the spin imbalance, yielding a larger net magnetization (Fig. 9d). This enhancement is caused by strong exchange interactions ($J_{p,3}^{mag}$ and $J_{p,4}^{mag}$; Table 1) between Fe layers in the hematite precipitate and Fe layers in the ilmenite host across interfaces normal to (001). Such interfaces are absent in the lower precipitate because it extends across the full width of the simulation cell. Since both lamellae have their net magnetic moments parallel to the blue spins (i.e., they are magnetically "in phase"), the total magnetic moment for the supercell is the sum of the magnetic moments on the two lamellae. The precipitates form in phase with each other in this case because the simulation was initialized with an ordered antiferromagnetic spin configuration throughout the supercell. If a random starting spin configuration were used, there is a 50:50 probability of the two precipitates being magnetized in opposite directions.

TABLE 2. Cation ordering (T_c), magnetic ordering (T_N), and exsolution (T_E) temperatures obtained from the simulations

x	T_c (K)	T_N (K)	T_E (K)
0		964(25)	
5		890(25)	675(25)
10		843(25)	750(25)
15		798(25)	775(25)
20		787(25)	800(25)
25		795(25)	800(25)
30		787(25)	825(25)
35		803(25)	850(25)
40		799(25)	875(25)
45		799(25)	912(25)
50		791(25)	975(25)
55		795(25)	1050(25)
60	1122(25)	784(25)	1050(25)
65	1175(25)	772(25)	1050(50)
70	1272(25)	769(25)	1000(25)
75	1370(25)	758(25)	975(25)
80	1460(25)	739(25)	900(25)
85	1531(25)	708(25)	825(25)
90	1612(25)	675(25)	750(25)
95	1637(25)	600(25)	650(25)
100	1663(25)		

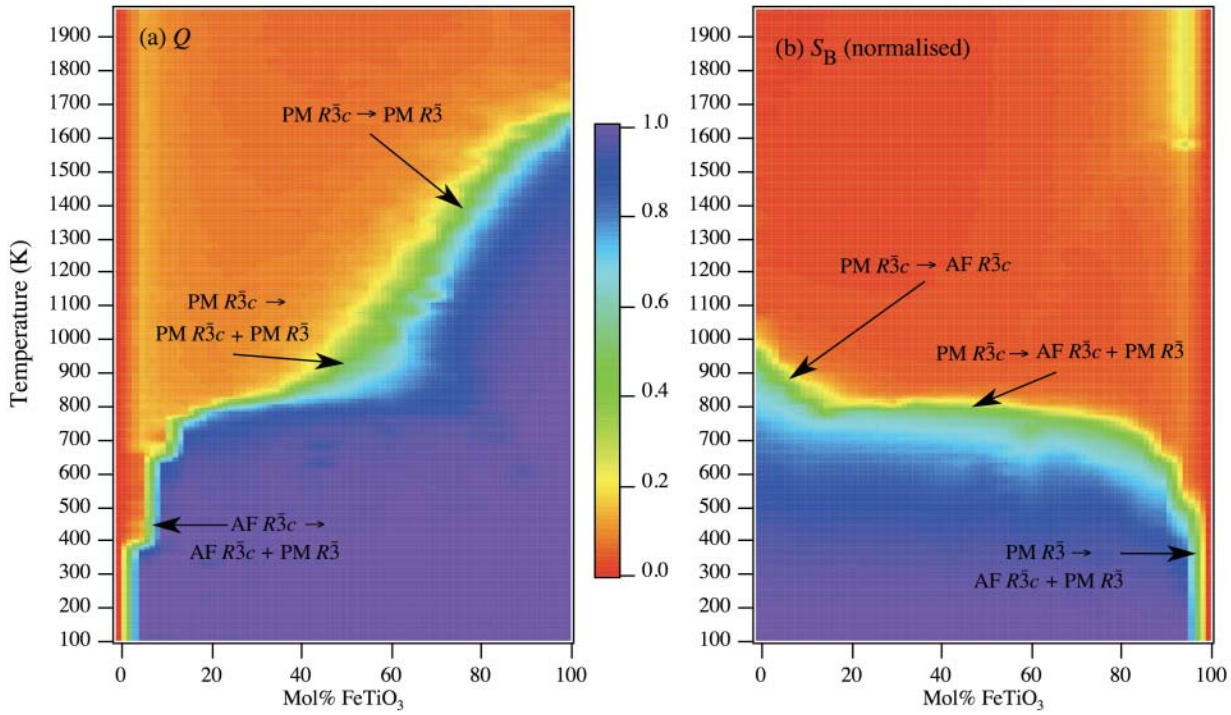

FIGURE 7. Image plots showing the variation in (**a**) cation order parameter, Q, and (**b**) sublattice spin, S_B, as a function of temperature and bulk composition for all simulations performed with the $4 \times 4 \times 8$ supercell. These plots can be used to track key features of the equilibrium phase diagram through temperature-composition space.

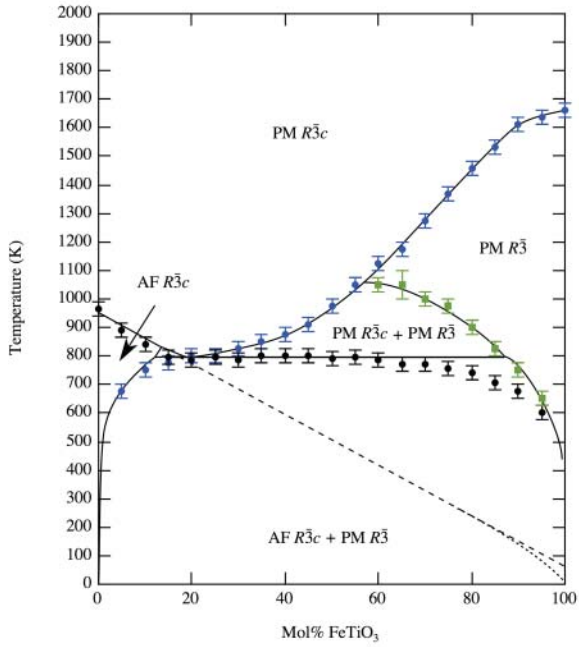

FIGURE 8. Summary of the equilibrium phase relations determined by Monte Carlo simulation (see also Table 2). Dashed and dotted lines show the metastable magnetic ordering temperatures for the cation-disordered and cation-ordered solid solution, respectively.

Internal structure of the contact layers

The contact layers adopt an ordered configuration of Fe^{3+} and Fe^{2+} cations (Fig. 10a). Fe^{3+} in the contact layer shares its octahedral face with Ti^{4+} in the layer below; Fe^{2+} in the contact layer shares its octahedral face with Fe^{3+} in the layer above. The possibility of Fe^{2+}-Fe^{3+} ordering within contact layers was first suggested by Robinson et al. (2004). They postulated an alternative ordering scheme whereby Fe^{3+} in the contact layer shares its octahedral face with Fe^{3+} in the layer above; Fe^{2+} in the contact layer shares its octahedral face with Ti^{4+} in the layer below (Fig. 10b). This alternative scheme is arguably more intuitive, since it maximizes the number of highly favorable Fe^{2+}-Ti^{4+} nearest neighbors (Table 1). The chemical energy of ordering schemes *a* and *b* in Figure 10 can be compared by summing the interactions around adjacent Fe^{2+} and Fe^{3+} cations in the contact layer:

$$E^{a}_{\text{chem}} = J^{\text{chem}}_{3,1} + J^{\text{chem}}_{2,1} + 5J^{\text{chem}}_{3,2} + 3J^{\text{chem}}_{1,3} + 3J^{\text{chem}}_{1,4} + 3J^{\text{chem}}_{3,4} + 3J^{\text{chem}}_{2,4} \quad (10)$$

$$E^{b}_{\text{chem}} = J^{\text{chem}}_{1,1} + 5J^{\text{chem}}_{3,2} + 3J^{\text{chem}}_{2,3} + 3J^{\text{chem}}_{3,3} + 3J^{\text{chem}}_{2,4} + 3J^{\text{chem}}_{1,4} + 3J^{\text{chem}}_{3,4} \quad (11)$$

yielding $E^{a}_{\text{chem}} = -10003$ K and $E^{b}_{\text{chem}} = -10052$ K. The magnetic contribution to the energy is (ignoring the weak double layer interactions):

$$E^{a}_{\text{mag}} = 2{\cdot}\frac{5}{2}{\cdot}J^{\text{mag}}_{3.1} + 5{\cdot}2{\cdot}\frac{5}{2}{\cdot}J^{\text{mag}}_{3.2} + 3{\cdot}\frac{5}{2}{\cdot}\frac{5}{2}{\cdot}J^{\text{mag}}_{1.3} + 3{\cdot}2{\cdot}\frac{5}{2}{\cdot}J^{\text{mag}}_{3.4} + 3{\cdot}\frac{5}{2}{\cdot}\frac{5}{2}{\cdot}J^{\text{mag}}_{1.4} \quad (12)$$

$$E^{b}_{\text{mag}} = \frac{5}{2}{\cdot}\frac{5}{2}{\cdot}J^{\text{mag}}_{1.1} + 5{\cdot}2{\cdot}\frac{5}{2}{\cdot}J^{\text{mag}}_{3.2} + 3{\cdot}2{\cdot}\frac{5}{2}{\cdot}J^{\text{mag}}_{3.3} + 3{\cdot}2{\cdot}\frac{5}{2}{\cdot}J^{\text{mag}}_{3.4} + 3{\cdot}\frac{5}{2}{\cdot}\frac{5}{2}{\cdot}J^{\text{mag}}_{1.4} \quad (13)$$

yielding $E^{a}_{\text{mag}} = -1982$ K and $E^{b}_{\text{mag}} = -1476$ K. In the absence of magnetic interactions, the chemical energy would favor the more intuitive ordering scheme *b* proposed by Robinson et al. (2004).

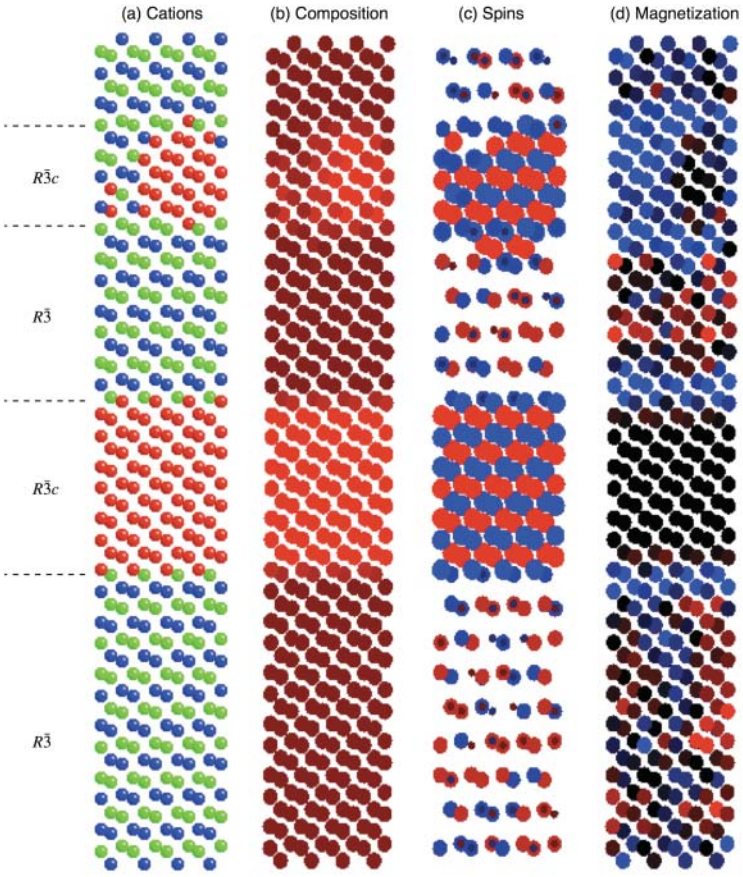

FIGURE 9. Snapshots of a combined simulation with $x = 0.7$, $T = 100$ K ($4 \times 4 \times 8$ supercell). (**a**) Distribution of Fe^{3+}, Fe^{2+}, and Ti^{4+} (red, green, and blue, respectively). (**b**) Local Fe concentration (bright red = hematite, dark red = ilmenite) calculated by averaging the number of Fe cations within the first four coordination shells around each site. (**c**) Magnitude and direction of spin for each site (red = negative, blue = positive; symbol size proportional to M_S). (**d**) Local ferrimagnetic moment (blue = positive, red = negative; brightness of color proportional to the magnitude of the net moment), calculated by averaging the spin values within the first 4 coordination shells around each site.

The presence of magnetic interactions, however, makes ordering scheme *a* significantly more energetically favorable. Preliminary calculations using Bond Valence Theory suggest that scheme *a* also provides more efficient charge satisfaction at the oxygen positions above and below the contact layer (Robinson et al. 2006a).

The presence of charge order within the contact layer has not yet been verified by either experimental or previous computational approaches. Burton et al. (2005) did not find any evidence for charge ordering using spin-polarized ab initio calculations. However, it should be reiterated that charge ordering within contact layers is *not* a prerequisite for lamellar magnetism; even if the extra electron associated with Fe^{2+} in the contact layers were evenly distributed through the hematite phase, an imbalance of spins—and a corresponding magnetic moment—would still be present. In fact, as demonstrated in Figure 9, small hematite-rich clusters with relatively disordered boundaries make a larger contribution to the net magnetization of the supercell than lamellae with atomically flat cation-ordered contact layers.

Temperature dependence of lamellar magnetism

The temperature dependence of sublattice magnetization, dS_A/dT and dS_B/dT, within the AF $R\bar{3}c$ + PM $R\bar{3}$ stability field is very different (Fig. 6). The sublattice with the smallest magnetization has $dS/dT = 0$ at 0 K, whereas the sublattice with the largest magnetization has a large negative dS/dT at 0 K. The difference in the initial rate of magnetic disordering leads to a rapid decrease in the net magnetization on heating. Above 400 K, the magnitude and temperature dependence of S_A and S_B become more similar.

Several factors contribute to the temperature dependence of lamellar magnetism: enhanced magnetic disordering of spins within the contact layers, textural evolution of the microstructure, and temperature-dependent changes in the partitioning of

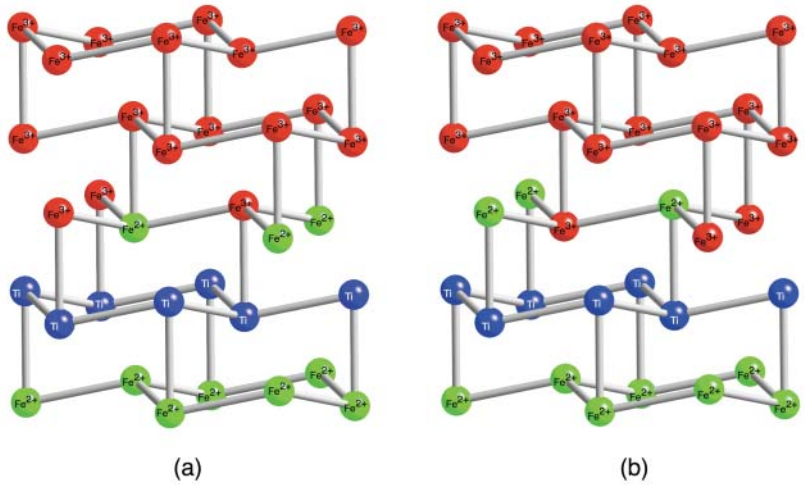

FIGURE 10. (**a**) Calculated arrangement of Fe^{2+} and Fe^{3+} cations within the contact layer in the combined simulations. Fe^{2+} in the contact layer shares its octahedral face with Fe^{3+} in the hematite layer above; Fe^{3+} in the contact layer shares its octahedral face with Ti^{4+} in the ilmenite layer below. (**b**) Alternative ordered arrangement proposed by Robinson et al. (2004). Fe^{2+} in the contact layer shares its octahedral face with Ti^{4+} in the ilmenite layer below; Fe^{3+} in the contact layer shares its octahedral face with Fe^{3+} in the hematite layer above. This ordering scheme would be observed in the absence of magnetic interactions.

cations at the interface. To assess the relative importance of these factors, a "magnetic only" simulation was performed using a supercell with bulk composition $x = 0.45$, pre-annealed at 125 K to generate an exsolution microstructure consisting of two ilmenite exsolution lamellae with well-defined flat interfaces. The cation configuration was held fixed in the simulation so only magnetic effects contribute to the temperature dependence of S_A and S_B. This method simulates the behavior that would be observed during laboratory heating of an exsolved sample, where cation diffusion is kinetically suppressed. The same difference in dS_A/dT and dS_B/dT is observed, leading to rapid reduction of net magnetization on heating to 400–500 K (Fig. 11). These results indicate that the dominant factor in controlling the temperature dependence of lamellar magnetism is the enhanced magnetic disordering of spins at the contact layers. This is a consequence of the fact that contact layer spins experience half as many interlayer interactions as bulk spins. This arrangement roughly halves the superexchange energy for ordering, resulting in a Néel temperature for the contact layer spins roughly half that of the bulk. Nevertheless, a small net magnetic moment is maintained right up to the Néel temperature of the hematite lamellae, indicating that exchange coupling of the contact layer spins to the bulk is maintained even at higher temperatures. Recent studies indicate that coherency strain may play a crucial role in stabilizing magnetic order in nanoscale lamellae (Dyar et al. 2004; McEnroe et al. 2002; Robinson et al. 2004). This may further enhance the net magnetization at temperatures above 500 K.

Simulation of antiphase domain microstructures

Samples cooled rapidly through the $R\bar{3}c$-$R\bar{3}$ transition develop a high degree of short-range cation order, characterized by the formation of fine-scale twin domains (Harrison and Redfern 2001; Nord and Lawson 1989, 1992). Twin domains form due to the loss of symmetry associated with the transition. Adjacent domains are related to each other by 180° rotation about the **a** axis and have an antiphase relationship with respect to the ordering of Fe and Ti layers; an Fe-rich layer becomes a Ti-rich layer on crossing the twin wall and vice versa. To emphasize this aspect, twin domains and twin walls will be referred to as antiphase domains (APDs) and antiphase domain boundaries (APBs), respectively, from now on. Domains with positive Q are referred to as "ordered," those with negative Q as "antiordered" (Eq. 5).

A starting configuration containing one ordered and one antiordered APD was generated by taking an $8 \times 8 \times 8$ supercell with fully ordered cation distribution and swapping the positions of Fe^{2+} and Ti^{4+} cations in the upper half. A combined simulation was then performed at some temperature below the $R\bar{3}c$-$R\bar{3}$ transition to "anneal" the system, allowing it to relax to a state of metastable equilibrium. After annealing, the cation configuration was frozen and "magnetic only" simulations were performed from 25–800 K.

Figure 12a shows the distribution of cations obtained after annealing a bulk composition of $x = 0.7$ at 850 K. The presence of antiphase domains is revealed in Figure 12b, which shows the local value of Q at each cation site (blue = positive, i.e., ordered; red = negative, i.e., antiordered; black = zero, i.e., disordered). The supercell consists of a fully ordered domain in the lower half and a fully antiordered domain in the upper half, with cation-disordered APBs in the center and at the bottom. The APBs are significantly enriched in Fe relative to the APDs (Fig. 12c). Although chemical heterogeneity is to be expected because the annealing temperature 850 K lies well within the PM $R\bar{3}c$ + PM $R\bar{3}$ miscibility gap, it is obviously favorable for the position of the APBs to coincide with regions of PM $R\bar{3}c$ exsolution. Such chemical segregation at APBs has been observed experimentally in natural pyroxenes using electon energy loss spectroscopic imaging (Moore et al. 2001), and the phenomenon of "wetting" at APBs is well discussed in the metallurgical literature (e.g., Cahn 2000). The magnetic structure obtained at 25 K is illustrated in Figure 12d. The alternating sequence of blue and red spins on adjacent cation layers is established uniformly throughout the supercell, regardless of the heterogeneities in cation order and bulk composition. The Fe-enriched APBs are well ordered magnetically. The Ti-enriched APDs are less well ordered magnetically. The net ferrimagnetic moments of the ordered and antiordered domains point in opposite directions (i.e., they are negatively exchange coupled) because their Fe-rich and Ti-rich layers are interchanged (i.e., Fe-rich layers in the ordered domain coincide with red spins, yielding a net magnetization parallel to the red spins, whereas Fe-rich layers in the antiordered domain

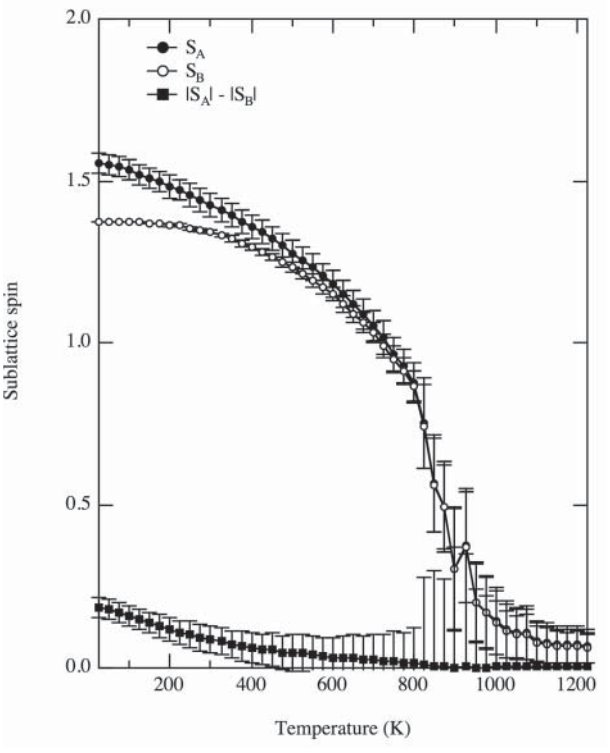

FIGURE 11. "Magnetic only" simulation with $x = 0.45$ ($4 \times 4 \times 8$ supercell), pre-annealed at 125 K to generate a microstructure consisting of two in-phase exsolution lamellae. Sublattice spins, S_A and S_B, are indicated by the closed and open cirlces, respectively. The net spin is indicated by the closed squares. Note the more rapid rate of decrease in net spin with temperature up to 500 K. A small net spin remains, however, up to the Néel temperature.

coincide with the blue spins, yielding a net magnetization parallel to the blue spins).

A quantitative analysis of the cation/spin configuration can be obtained by calculating the average values of order parameter, composition, and spin on each of the 48 layers in the supercell (Figs. 13a–13d). The ordered and antiordered domains are fully cation ordered ($Q = \pm 1$) over a distance of ~12 cation layers (2 unit cells) and are joined by APB regions where Q varies from –1 to +1 over a similar distance (Fig. 13a). This order parameter profile corresponds to a material with a high degree of short-range cation order and a low degree of long-range cation order (i.e., the average value of Q over the whole supercell is close to zero). The average composition at the center of the APDs is 0.89 (Fig. 13b), slightly more ilmenite-rich than the value of 0.83 predicted by the equilibrium phase diagram (Fig. 8). The average composition at the center of the APBs is $x = 0.36$, close to the value of 0.35 predicted by the equilibrium phase diagram. Note, however, that the phase diagram is based on simulations that are the average of several million configurations. Here we are examining a single snapshot that may deviate significantly from the thermodynamic average. Nevertheless, it is clear that the compositional heterogeneity at this temperature is driven by unmixing rather than some special property of the APBs. The spin profile at 25 K shows the presence of oppositely magnetized ferrimagnetic domains (indicated by the arrows in Fig. 13c). This negative coupling is mediated by exchange interactions through the APB. The boundary region is characterized by an asymmetric spin profile with a smoothly varying ferrimagnetic moment that changes sign at its center. Only the very center of the APB can be classed as antiferromagnetic. At 400 K, the ferrimagnetic domains are paramagnetic but the APBs retain a narrow region of magnetic order (Fig. 13d).

To test whether chemical heterogeneity also can be generated by APBs in the absence of a miscibility gap, simulations have been performed at a range of temperatures within the single-phase PM $R\bar{3}$ stability field. Representative results for an annealing temperature of 1100 K are shown in Figures 13e–13h. The supercell contains a well-ordered domain with a flat order parameter profile and a less well-(anti)ordered domain with a curved order parameter profile (Fig. 13e). This corresponds to an intermediate state in the transition from short- to long-range order (i.e., the value of Q averaged over the whole supercell is non-zero). The heterogeneities in Q are accompanied by significant heterogeneities in composition (Fig. 13f). There is evidence of slight Fe enrichment at the APBs. However, a more important result is the partitioning of Fe between the domains themselves: the well-ordered domain has $x > 0.7$, whereas the less well-(anti)ordered domain has $x < 0.7$. The spin profile at 25 K indicates a strong ferrimagnetic moment associated with the ordered domain and a weak ferrimagnetic moment with the antiordered domain (Fig. 13g). At 375 K, magnetic order is lost in the ordered domain, whereas weak magnetic order is retained across the antiordered domain and boundary regions (Fig. 13h).

The variation in S_A and S_B vs. T for both the 850 and 1100 K microstructures is shown in Figure 14. For the 850 K simulation, magnetic ordering sets in below 600 K (Fig. 14a). This corresponds to T_N for the Fe-enriched APBs with $x = 0.36$ (Fig. 8). S_A and S_B differ slightly, resulting in a small net magnetic moment that increases in magnitude on cooling. Magnetic ordering in the ferrimagnetic APDs sets in below 150 K. This is accompanied by a small decrease in the net magnetic moment. No large ferrimagnetic moment is generated in the supercell as a whole due to the negative exchange coupling between the APDs, which leads to cancellation of their net moments. No reversal of the net magnetization is observed down to 25 K. For the 1100 K simulation, magnetic ordering sets in below 425 K. This corresponds to the onset of magnetic ordering in the Fe-enriched antiordered domain. The weak ferrimagnetic moment of the antiordered domain reaches a maximum at 350 K and then starts to decrease as magnetic order spreads to the surrounding regions. By 250 K, the moment of the antiordered domain is cancelled out by the oppositely oriented moment of the boundary regions and the ordered domain. Below 250 K, the net magnetic moment is dominated by the strong ferrimagnetic moment of the ordered domain and is reversed with respect to the net moment obtained above 250 K.

Discussion

Mechanism of self-reversed thermoremanent magnetization

The mechanism of self-reversed thermoremanent magnetization (SR-TRM) has been hotly debated ever since its discovery in the Haruna dacite by Nagata et al. (1951). A common requirement of all models is the presence of at least two phases: a weakly magnetic metastable phase with a high Néel temperature and a strongly magnetic stable phase with a low Néel temperature. The metastable phase is referred to often as the "*x*-phase" (first proposed by Ishikawa and Syono 1963). This is the first phase to order magnetically on cooling, acquiring a normal TRM in the presence of an applied field. The stable phase orders magnetically at a lower temperature and is forced to acquire a reversed TRM due to negative exchange coupling to the *x*-phase. Much of the debate regarding SR-TRM has focussed on the nature of the *x*-phase and the origin of the negative exchange coupling. Nord and Lawson (1989, 1992) demonstrated a correlation between the size of APDs and the occurrence of SR-TRM, and suggested that Fe-enriched cation-disordered antiferromagnetic APBs act as the *x*-phase. Others support the hypothesis that the *x*-phase is partially cation ordered and hence ferrimagnetic (Ishikawa and Syono 1963; Prévot et al. 2001). The weakly magnetic nature of the *x*-phase makes it difficult to detect in macroscopic magnetic measurements. The problem is exacerbated by the absence of any quantitative understanding of the coupling between magnetic and cation ordering at the nanometer scale.

This study provides the first quantitative insight into the temperature-dependent cation/spin configuration in quenched ilmenite-hematite. The simulations reveal a clear correlation between the local composition and the local degree of cation order—a key requirement of most SR-TRM models. Symmetry dictates that the composition, x, couples to an even power of the cation order parameter, Q. The best linear correlation for the simulation at 850 K (i.e., below the miscibility gap) was obtained by plotting x vs. Q^4 (Fig. 15a, $r = 0.92$). The best linear correlation for the simulation at 1100 K (i.e., above the miscibility gap) was obtained by plotting x vs. Q^2 (Fig. 15b, $r = 0.77$). The conclusion is that ordered and antiordered APDs will differ in composition

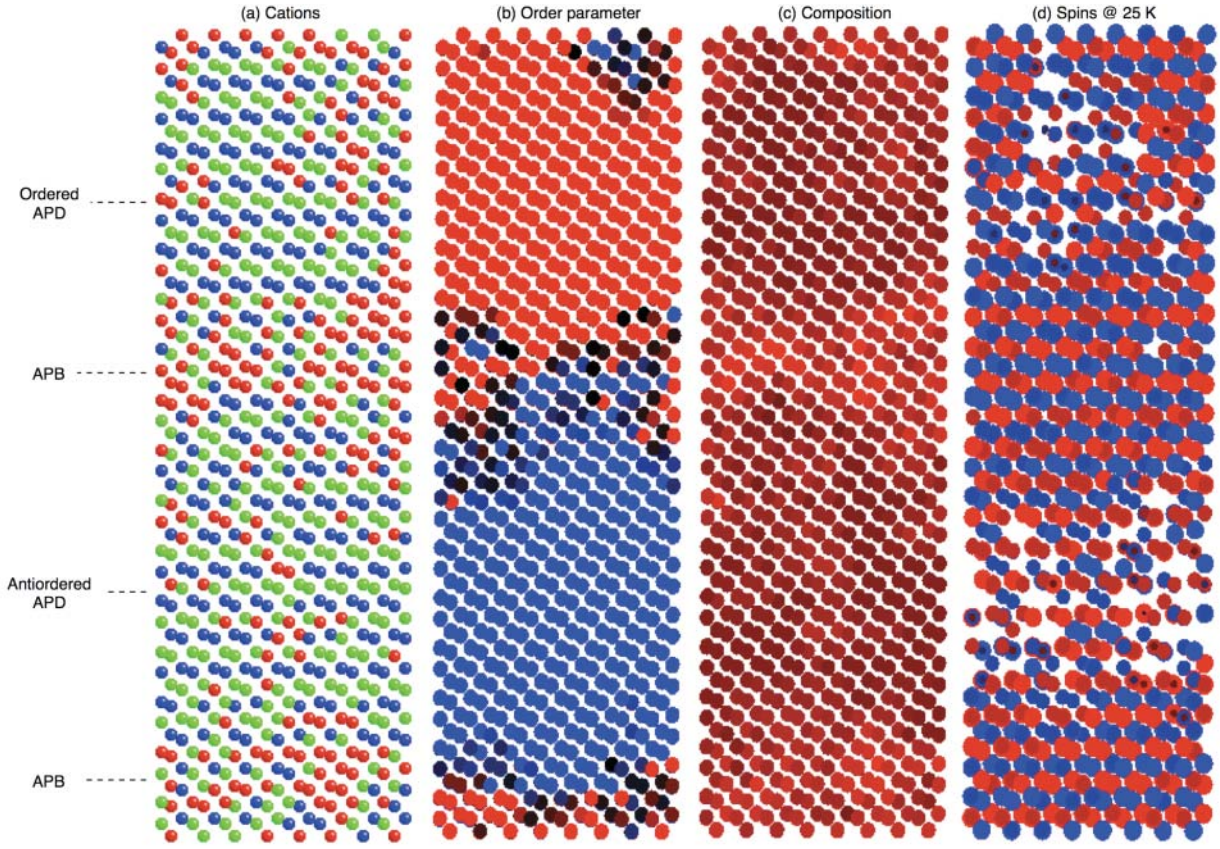

FIGURE 12. Snapshots of antiphase domains (APDs) and antiphase domain boundaries (APBs) formed in a combined simulation with $x = 0.7$ at $T = 850$ K ($8 \times 8 \times 8$ supercell). (**a**) Distribution of Fe^{3+}, Fe^{2+}, and Ti^{4+} (red, green, and blue, respectively). (**b**) Local cation order parameter, Q, (blue = positive, i.e., ordered; red = negative, i.e., antiordered; black = zero, i.e., disordered) calculated by determining the Ti^{4+} concentration on adjacent layers within the first four coordination shells around each site. (**c**) Local Fe concentration (bright red = hematite-rich, dark red = ilmenite-rich) calculated by determining the total Fe concentration within the first four coordination shells around each site. (**d**) Magnitude and direction of spin for each site (red = negative, blue = positive; symbol size proportional to M_S).

if their absolute values of Q are different.

The transition from short- to long-range cation order in quenched Ilm_{60} and Ilm_{65} has been examined using neutron diffraction (Harrison and Redfern 2001). Freshly quenched Ilm_{60} and Ilm_{65} contain ordered and antiordered domains with diameters of the order 2–10 nm. The degree of cation order within the domains was found to be very high ($|Q| \sim 1$), but the overall degree of long-range cation order low ($<Q> \sim 0$). This state is illustrated schematically in Figure 16a. Annealing within the PM $R\overline{3}$ stability field drives the system to an equilibrium state of homogeneous long-range cation order. This can be achieved by a simple coarsening mechanism, whereby the ordered domains in one region of the crystal grow at the expense of the antiordered domains (Fig. 16b). In adjacent regions the antiordered domains grow at the expense of the ordered domains, leading to a larger scale domain structure superimposed on the fine-scale heterogeneities. Eventually, the dominant domains in each region join up to form homogeneous APDs (Fig. 16d). Repetition of this process leads to further coarsening. An alternative to coarsening would be the order-disorder mechanism, whereby Q gradually changes sign in one set of domains, while keeping the size of the domains constant (Fig. 16c). Since the APBs are of finite width, it is more realistic to envisage a combined mechanism (Fig. 16d). As APBs start to impinge during coarsening, overlap of their order-parameter profiles will lead to a decrease in the degree of order (e.g., Fig. 13e). This is accompanied by Fe enrichment across the two encroaching APBs and the poorly (anti)ordered domain sandwiched in-between (Fig. 13f). These enriched regions fulfill all the requirements of Ishikawa's x-phase: they are the first regions to become magnetically ordered on cooling (Figs. 13h); they are very close to being antiferromagnetic, but carry a small net moment due to the partial cation order of antiordered domain (Fig. 14b); they are negatively exchanged coupled to the ordered APDs on both sides (Fig. 13g); and they are metastable, only appearing in systems that are part way through the transformation from short- to long-range order.

Experimental evidence in support of this model can be obtained from transmission electron microscopy (Nord and Lawson 1992). According to Figure 16d, the microstructure of self-reversing ilmenite-hematite should consist of fine-scale heterogeneities in x and Q superimposed on much larger scale APDs. Nord and Lawson (1992) noted the presence of a "mottled

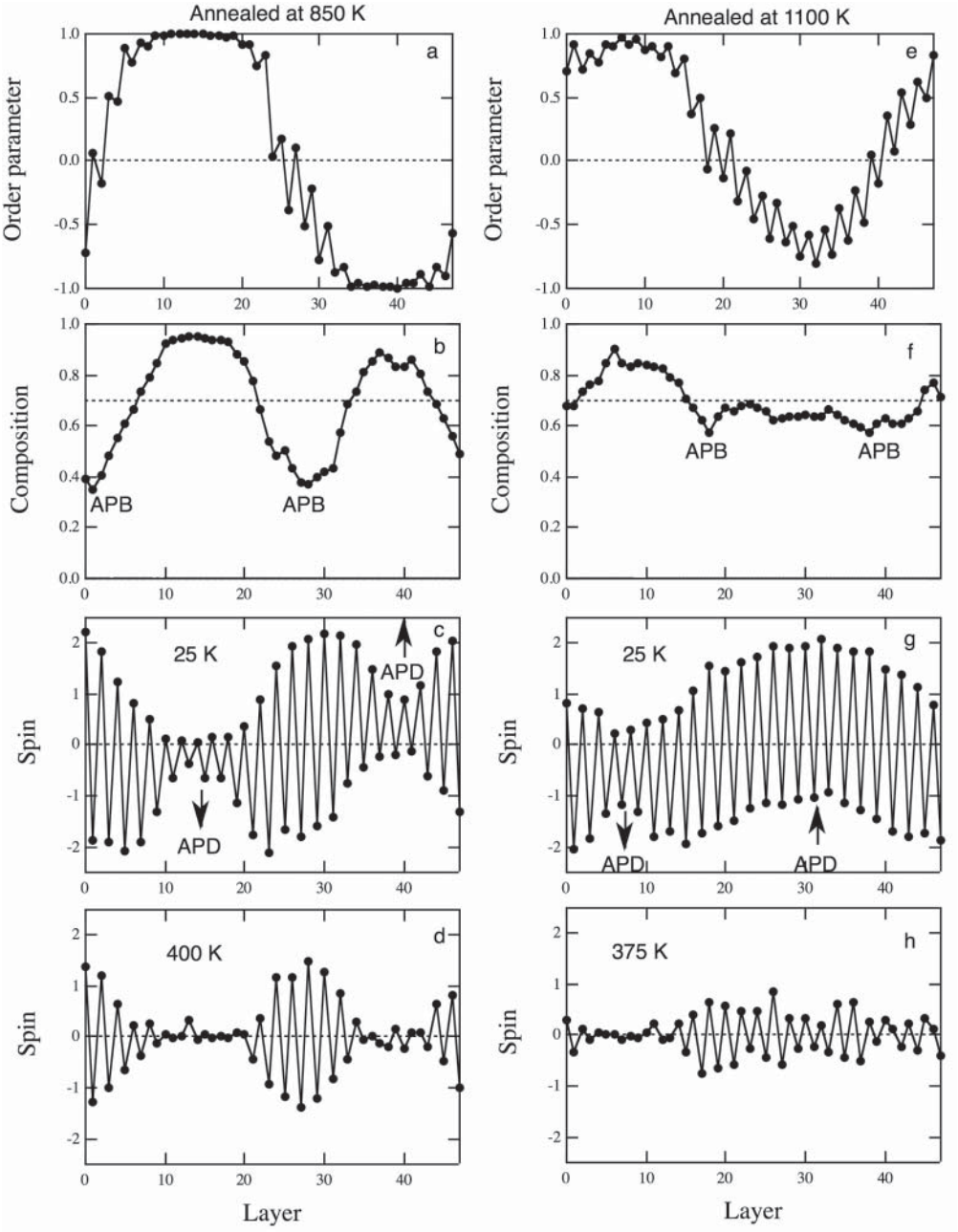

FIGURE 13. Average values of order parameter, composition, and spin on each of the 48 layers of an $8 \times 8 \times 8$ supercell with $x = 0.7$, pre-annealed at (**a–d**) 850 K (see Fig. 12) and (**e–h**) 1100 K. A starting configuration with APBs at the bottom and the center of the supercell was chosen in each case. (**a**) The order parameter profile at 850 K shows two fully ordered/antiordered APDs ($Q = 1$ and $Q = -1$, respectively) separated by APBs ($Q = 0$). (**b**) The composition profile at 850 K shows that unmixing has taken place within the PM $R\bar{3}c$ + PM $R\bar{3}$ miscibility gap, with the PM $R\bar{3}$ phase corresponding to the APDs and the PM $R\bar{3}c$ phase corresponding to the APBs. Dashed line indicates the bulk composition, $x = 0.7$. (**c**) The spin profile at 25 K shows that the APDs are strongly ferrimagnetic. The APD centered on layer 14 has a net negative spin, whereas the APD centered on layer 40 has a net positive spin (indicated by the arrows). (**d**) The spin profile at 400 K shows that the Fe-rich APBs remain magnetically ordered, whereas the Fe-poor APDs are magnetically disordered. The APBs are associated with a small net spin (see Fig. 14). (**e**) The order parameter profile at 1100 K shows a fully ordered APD ($Q \sim 1$) and a less well (anti)ordered APD ($Q \sim -0.75$). (**f**) The composition profile at 1100 K shows that the well ordered APD has $x > 0.7$, whereas the less well ordered APD has $x < 0.7$. Evidence for Fe enrichment at the APBs is also seen. (**g**) The spin profile at 25 K shows that the well ordered APD is strongly ferrimagnetic, whereas the ferrimagnetic spin of the less well ordered APD is decreased by the influence of the boundary regions. (**h**) The spin profile at 375 K shows that the less well-ordered APD and boundary regions are magnetically ordered, whereas the well-ordered APD is magnetically disordered. The magnetically ordered regions carry a small net spin that is opposite to the net spin of the well-ordered APD (see Fig. 14).

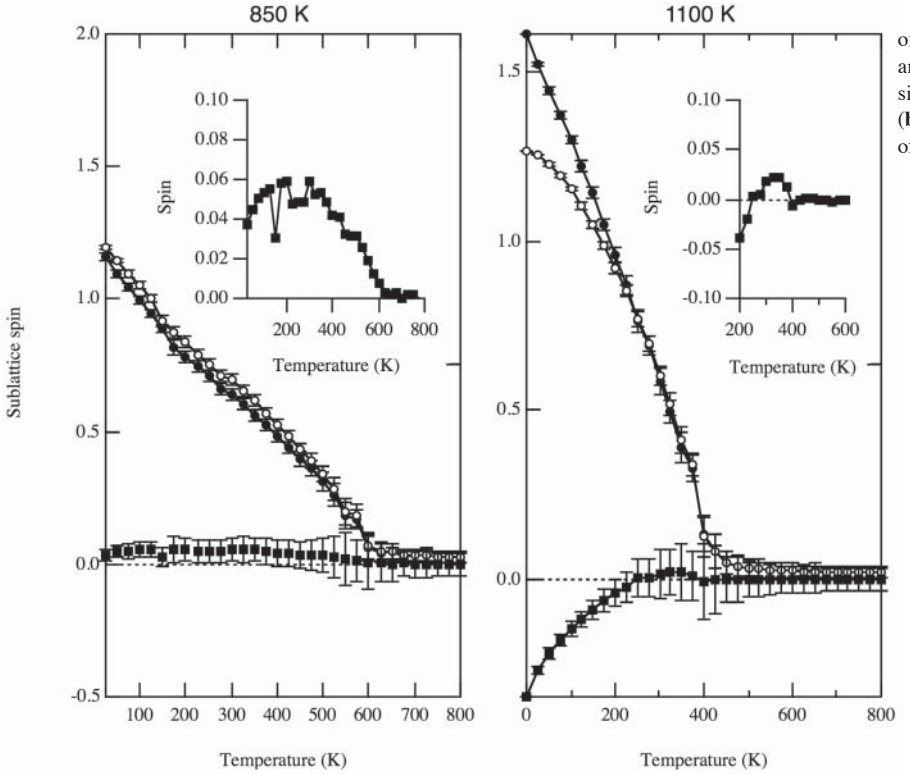

FIGURE 14. Temperature dependence of sublattice spins S_A and S_B (circles) and net spin $|S_A|-|S_B|$ (squares) for the simulations pre-annealed at (**a**) 850 and (**b**) 1100 K. Insets show expanded view of the variation in net spin.

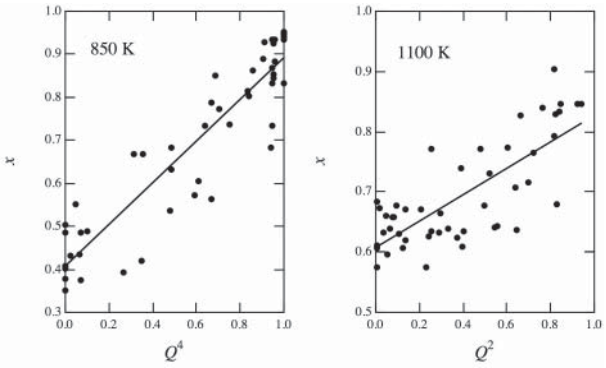

FIGURE 15. Correlation plot of local composition, x, vs. local order parameter, Q^4 or Q^2, for the simulations performed at (**a**) 850 and (**b**) 1100 K.

background" in their quenched samples, that appeared under the same imaging conditions as the larger scale APDs. This mottling was interpreted as evidence for heterogeneous ordering and/or compositional fluctuations within the APDs. The mottling disappears after prolonged annealing, consistent with it being a metastable feature of rapidly cooled samples. More significantly, it was noted that the mottled texture was present in all samples that acquired SR-TRM but absent from samples that acquired normal TRM. To investigate this further, new TEM observations have been made of a synthetic sample of Ilm_{70} (Fig. 17). The sample was synthesized under controlled f_{O_2} at 1300 °C (Harrison et al. 2000b), quenched into water, sealed in an evacuated silica tube, and annealed for 100 h at 650 °C. The microstructure is heterogeneous on a very fine length scale (Fig. 17a). Closer examination reveals the presence of mottled regions consisting of ~4–8 nm diameter white spots with spacing ~10–20 nm. The mottling is superimposed on a larger-scale microstructure consisting of ~100 nm wide APDs separated by meandering APBs. The length scale of the mottling agrees well with the length scale of the cation ordering heterogeneities identified by neutron diffraction (Harrison and Redfern 2001). Although the remanence properties of this particular sample have not been measured, the observed microstructure is similar to that identified by Nord and Lawson (1992) in samples that displayed SR-TRM.

Limitations of the simulations

The energetic model described in this paper successfully describes many of the known thermodynamic and magnetic properties of the ilmenite-hematite solid solution, and is able to provide new and valuable insight into the interaction between magnetism and microstructure. The strength of the model is its simplicity—with relatively few empirical parameters describing the chemical and magnetic interactions, it is easy to understand what contribution each parameter makes to the observed behavior. These parameters may be refined in the future, as new magnetic and cation ordering data are acquired. In particular, improved values for Fe^{2+}-Fe^{3+} and Fe^{2+}-Fe^{2+} interactions in ilmenite-rich compositions are urgently needed. The model currently underestimates the strength of the double layer Fe^{2+}-Fe^{2+} interactions, with the result that the Néel temperature of pure cation-ordered ilmenite is underestimated significantly. Without an improved estimate of this parameter, the model is unable to provide insight into the competing interactions that lead to the suppression

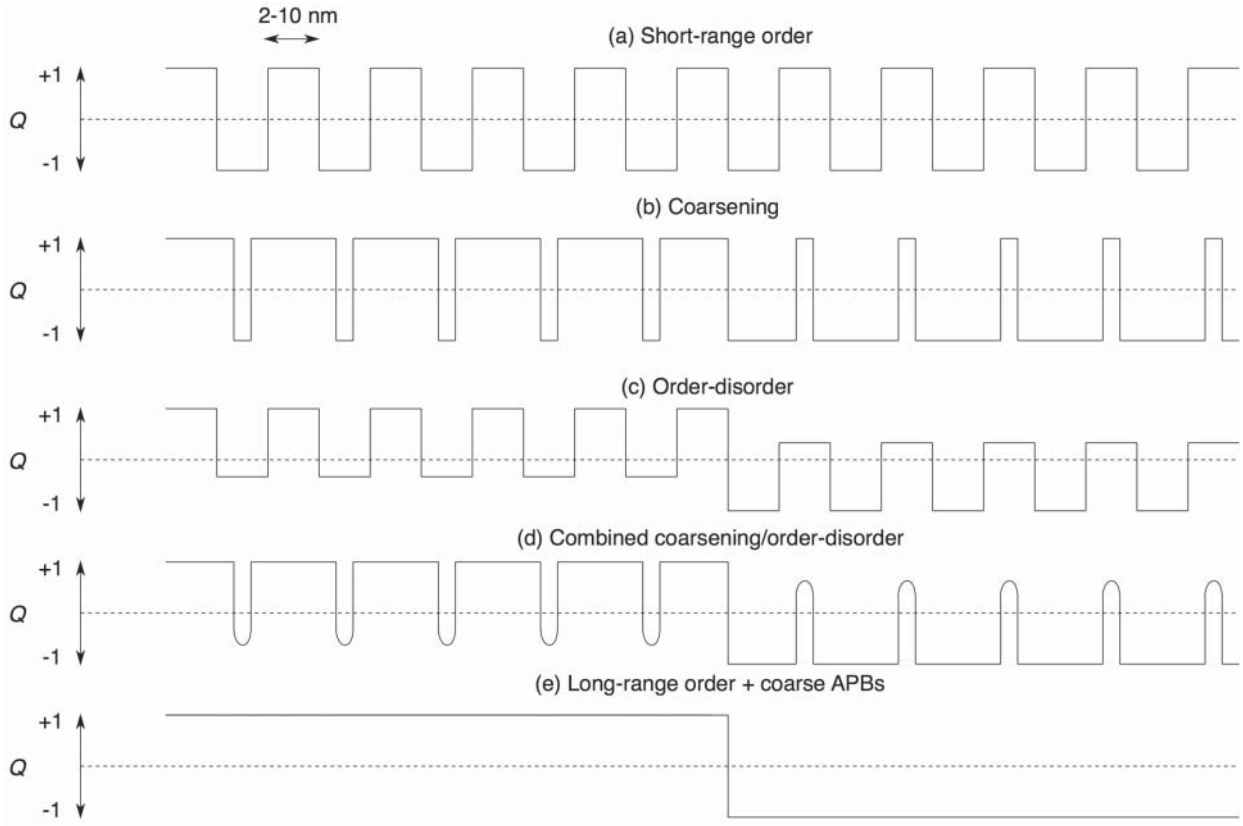

FIGURE 16. Schematic illustration of possible mechanisms for the transformation from short- to long-range cation order. (**a**) Short-range cation order in quenched ilmenite-hematite is characterised by a fine scale altneration of ordered ($Q = 1$) and antiordered ($Q = -1$) domains with $<Q> = 0$. The length scale of these domains in ilm60 is 2–10 nm, as revealed by neutron diffraction (Harrison and Redfern 2001). (**b**) Coarsening leads to the growth of ordered domains at the expense of antiordered domains in one region of the crystal (left hand side) and growth of antiordered domains at the expense of ordered domains in adjacent regions (right hand side). Each region now has $<Q> > 0$. (**c**) Disordering of the antiordered domains in one region leads to $<Q> > 0$. (**d**) A combination of coarsening plus disordering as the APBs impinge leads to an order parameter profile similar to that seen in Figure 13e. (**e**) Long-range cation order with coarse APDs.

of long-range magnetic order in the spin-glass region. Proper treatment of magnetic ordering in this region would also have to account for the different magnetocrystalline anisotropies of hematite and ilmenite. This would require the development of a classical or quantum mechanical Heisenberg model, rather than the more simplistic multistate Potts model adopted here.

The price of simplicity is that certain aspects of the cation- and magnetic-ordering behavior are neglected. Most obvious is the need to account for spin canting. Although the energy of the interactions causing spin canting is negligible, it is the dominant source of magnetization in the cation-disordered solid solution. The possible influence of spin canting on lamellar magnetism was discussed by Robinson et al. (2004) and Robinson et al. (2006). It is envisaged that any NRM acquired by exsolved ilmenite-hematite would be the vectorial sum of the spin-canted moment (which lies within the basal plane and perpendicular to the alignment of the spins) and the lamellar moment (which also lies in the basal plane but is parallel to the alignment of spins). Given that the lamellar moment far outweighs the spin-canted moment, we expect only a small rotation of the NRM direction away from the direction of spin alignment. Neutron diffraction experiments to determine the magnitude of this deflection are currently underway.

Given the weakly magnetic nature of the *x*-phase, spin canting is likely to have a greater influence on the mechanism of SR-TRM than on lamellar magnetism. Without detailed knowledge of the interactions that cause spin canting—and their dependence on *x* and *Q*—it is difficult to see how the current model could be adapted sensibly. Hence, other than providing an arguably more intuitive explanation of SR-TRM, the current model cannot be used to rule out the spin-rotation model proposed by Hoffman (1992). It does, however, go a long way toward addressing the need for a quantitative analysis of the heterogeneous state of cation and magnetic order in rapidly cooled samples, and a solid foundation for understanding of the nature of exchange coupling at APBs.

ACKNOWLEDGMENTS

This research was supported by grants from the Research Council of Norway (grant 163556, "The nature and origin of natural magnetic nanoscale materials" to S. McEnroe) and by a NERC Advanced Fellowship (NE/B501339/1, "Mineral magnetism at the nanometre scale" to R.J. Harrison). The work on lamellar magnetism has benefited enormously from on-going collaborations and discussions with Peter Robinson and Suzanne McEnroe.

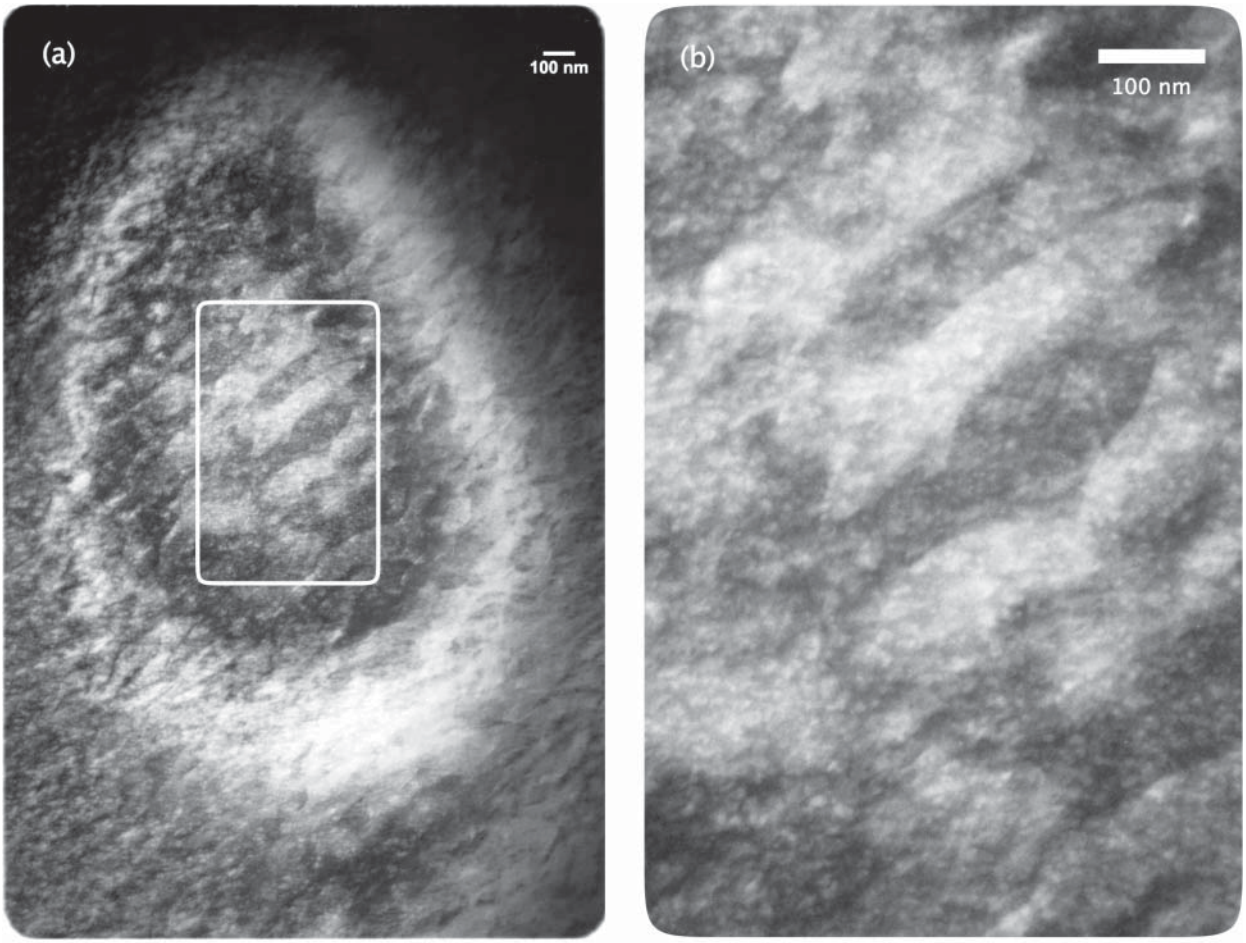

FIGURE 17. Dark-field TEM image of the fine-scale domain structure observed in a sample with $x = 0.7$ quenched from 1300 °C and then annealed at 650 °C for 10 h. The image in (**b**) is a blow up of the region indicated in **a**. The microstructure consists of fine scale heterogeneities (~4–8 nm diameter spots with spacing ~10–20 nm) superimposed on larger-scale (~100 nm wide) APDs. The length scale and type of microstructure is consistent with the mechanism of transformation from short- to long-range cation order proposed in Figure 16. White ring in **a** is caused by the focusing-down of the electron beam on the specimen.

REFERENCES CITED

Arai, M. and Ishikawa, Y. (1985) A new oxide spin glass system of (1-x)$FeTiO_3$–xFe_2O_3. III. Neutron scattering studies of magnetization processes in a cluster type spin glass of 90$FeTiO_3$–10Fe_2O_3. Journal of the Physical Society of Japan, 54, 795–802.

Arai, M., Ishikawa, Y., Saito, N., and Takei, H. (1985a) A new oxide spin glass system of (1-x)$FeTiO_3$–xFe_2O_3. II. Neutron scattering studies of a cluster type spin glass of 90$FeTiO_3$–10Fe_2O_3. Journal of the Physical Society of Japan, 54, 781–794.

Arai, M., Ishkawa, Y., and Takei, H. (1985b) A new oxide spin glass system of (1-x)$FeTiO_3$–xFe_2O_3. IV. Neutron scattering studies on a reentrant spin glass of 79$FeTiO_3$–21Fe_2O_3 single crystal. Journal of the Physical Society of Japan, 54, 2279–2286.

Becker, U., Fernandez-Gonzalez, A., Prieto, M., Harrison, R.J., and Putnis, A. (2000) Direct calculation of the mixing enthalpy of the barite/celestite system. Physics and Chemistry of Minerals, 27, 291–300.

Bina, M., Tanguy, J.C., Hoffmann, V., Prévot, M., Listanco, E.L., Keller, R., Fehr, K.T., Goguitchaichvili, A., and Punongbayan, R.S. (1999) A detailed magnetic and mineralogical study of self-reversed dacitic pumices from the 1991 Pinatubo eruption (Philippines). Geophysical Journal International, 138, 159–178.

Bosenick, A., Dove, M.T., and Geiger, C.A. (2000) Simulation studies of pyrope–grossular solid solutions. Physics and Chemistry of Minerals, 27, 398–418.

Bosenick, A., Dove, M.T., Myers, E.R., Palin, E.J., Sainz-Diaz, C.I., Guiton, B.S., Warren, M.C., Craig, M.S., and Redfern, S.A.T. (2001) Computational methods for the study of energies of cation distributions: applications to cation-ordering phase transitions and solid solutions. Mineralogical Magazine 65, 193–219.

Burton, B.P. and Davidson, P.M. (1988) Multicritical phase relations in minerals. In E.S.S. Ghose, J.M.D. Coey, and E. Salje, Eds., Structural and Magnetic Phase Transitions in Minerals, Advances in Physical Geochemistry, 7, p. 60–90. Springer Verlag, Berlin.

Burton, B. and Kikuchi, R. (1984) Thermodynamic analysis of the system $CaCO_3$-$MgCO_3$ in the tetrahedron approximation of the cluster variation method. American Mineralogist, 69, 165–175.

Burton, B.P., Chaka, A., and Singh, D.J. (2005) Chemical, magnetic and charge ordering in the system hematite-ilmenite, Fe_2O_3-$FeTiO_3$. Phase Transitions, 78, 239–249.

Cahn, J.W. (2000) Wetting and non-wetting near critical points in solids. Physica A, 279, 195–202.

Dove, M.T. (2001) Computer simulations of solid solutions. In C. Geiger, Ed., Solid Solutions in Silicate and Oxide Systems of Geological Importance. EMU Notes in Mineralogy, 16, 57–64.

Dunlop, D.J. and Özdemir, Ö. (1997) Rock Magnetism: Fundamentals and Frontiers. Cambridge University Press, Cambridge.

Dyar, D.M., McEnroe, S.A., Murad, E., Brown L.L., and Schiellerup, H. (2004) The relationship between exsolution and magnetic properties in hemo-ilmenite: Insights from Mössbauer spectroscopy. Geophysical Research Letters, 31, L04608. DOI:10.1029/2003GL019076

Ghiorso, M.S. (1997) Thermodynamic analysis of the effect of magnetic ordering on miscibility gaps in the FeTi cubic and rhombohedral oxide minerals and the FeTi oxide geothermometer. Physics and Chemistry of Minerals, 25, 28–38.

Harrison, R.J. (2000) Magnetic transitions in Minerals. In S.A.T. Redfern and M.A. Carpenter, Eds., Trnasformation Processes in Minerals, 39, 175–202. Reviews in Mineralogy and Geochemistry, Mineralogical Society of America, Chantilly, Virginia.

Harrison, R.J. and Becker, U. (2001) Magnetic ordering in solid solutions. In C. Geiger, Ed., Solid solutions in silicate and oxide systems, 3, 349–383. European Mineralogical Society Notes in Mineralogy, Eötvös University Press, Budapest.

Harrison, R.J. and Redfern, S.A.T. (2001) Short- and long-range ordering in the ilmenite-hematite solid solution. Physics and Chemistry of Minerals, 28, 399–412.

Harrison, R.J., Becker, U., and Redfern, S.A.T. (2000a) Thermodynamics of the $R\bar{3}$ to $R\bar{3}c$ phase transition in the ilmenite-hematite solid solution. American Mineralogist, 85, 1694–1705.

Harrison, R.J., Redfern, S.A.T, and Smith, R.I. (2000b) In-situ study of the $R\bar{3}$ to $R\bar{3}c$ phase transition in the ilmenite-hematite solid solution using time-of-flight neutron powder diffraction. American Mineralogist, 85, 194–205.

Hauptman, Z. (1974) High-temperature oxidation, range of non-stoichiometry, and Curie point variation of cation deficient titanomagnetite $Fe_{2.4}Ti_{0.6}O_{4+\gamma}$. Geophysical Journal of the Royal Astronomical Society, 38, 29–47.

Hoffman, K.A. (1992) Self-reversal of thermoremanent magnetization in the ilmenite-hematite system: Order-disorder, symmetry, and spin alignment. Journal of Geophysical Research, 97, 10883–10895.

Ishikawa, Y. (1958) An order-disorder transformation phenomenon in the Fe_2O_3-$FeTiO_3$ solid solution series. Journal of the Physical Society of Japan, 13, 828–837.

——— (1962) Magnetic properties of the ilmenite-hematite system at low temperature. Journal of the Physical Society of Japan, 17, 1835–1844.

——— (1964) Superparamagnetsm in magnetically dilute systems. Journal of Applied Physics, 35, 1054–1059.

Ishikawa, Y. and Akimoto, S. (1957) Magnetic properties of the $FeTiO_3$-Fe_2O_3 solid solution series. Journal of the Physical Society of Japan, 12, 1083–1098.

Ishikawa, Y. and Syono, Y. (1963) Order-disorder transformation and reverse thermoremanent magnetization in the $FeTiO_3$-Fe_2O_3 system. Journal of the Physics and Chemistry of Solids, 24, 517–528.

Ishikawa, Y., Saito, N., Arai, M., Watanabe, Y., and Takei, H. (1985) A new oxide spin glass system of (1-x)$FeTiO_3$–xFe_2O_3. I. Magnetic properties. Journal of the Physical Society of Japan, 54, 312–325.

Kasama, T., McEnroe, S.A., Ozaki, N., Kogure, T., and Putnis, A. (2004) Effects of nanoscale exsolution in hematite-ilmenite on the acquisition of stable natural remanent magnetization. Earth and Planetary Science Letters, 224, 461–475.

Lagroix, F., Banerjee, S.K., and Moskowitz, B.M. (2005) Revisiting the mechanism of reversed thermoremanent magnetization based on observations from synthetic ferrian ilmenite (y = 0.7). Journal of Geophysical Research, 109, B12108. DOI:10.1029/2004JB003076

McEnroe, S.A., Harrison, R.J., Robinson, P. Golla, U., and Jercinovic, M.J. (2001) The effect of fine-scale microstructures in titanohematite on the acquisition and stability of NRM in granulite facies metamorphic rocks from Southwest Sweden: Implications for crustal magnetism. Journal of Geophysical Research, 106, 30523–30546.

McEnroe, S.A., Harrison, R.J., Robinson, P., and Langenhorst, F. (2002) Nanoscale hematite-ilmenite lamellae in massive ilmenite rock: an example of "Lamellar Magnetism" with implications for planetary magnetic anomalies. Geophysical Journal International, 151, 890–912.

McEnroe, S.A. Langenhorst, F., Robinson P., Bromiley G., and C. Shaw (2004a) What's magnetic in the lower Crust? Earth and Planetary Science Letters, 226, 175–192.

McEnroe, S.A., Brown L.L., and Robinson, P. (2004b) Earth analog for Martian magnetic anomalies: Remanence properties of hemo-ilmenite norites in the Bjerkreim-Sokndal Intrusion, Rogaland, Norway. Journal of Applied Geophysics, 56/3, 195–212.

McEnroe, S.A., Skilbrei, J.R., Robinson, P., Heidelbach, F., Langenhorst, F., and Brown, L.L. (2004c) Magnetic anomalies, layered intrusions and Mars. Geophysical Research Letters, 31, L19601. DOI:10.1029/2004GL020640

Moore, K.T., Veblen, D.R., and Howe, J.M. (2001) Calcium segregation at antiphase boundaries in pigeonite. American Mineralogist, 86, 1314–1318.

Morrish, A.H. (1994) Canted antiferromagnetism: hematite. World Scientific Publishing Co., Singapore.

Mouritsen, O.G. (1984) Computer studies of phase transitions and critical phenomena. Springer-Verlag, Berlin.

Nagata, T., Akimoto, S., and Uyeda, S. (1951) Reverse thermo-remanent magnetism, Proceedings of the Japan Academy, 27, 643–645.

Nord, G.L. and Lawson, C.A. (1989) Order-disorder transition-induced twin boundaries and magnetic properties in ilmenite-hematite. American Mineralogist, 74, 160–176.

——— (1992) Magnetic properties of ilmenite70-hematite: Effects of transformation-induced twin boundaries. Journal of Geophysical Research, 97, 10897–10910.

Phillips, B.L., Kirkpatrick, R.J., and Carpenter, M.A. (1992) Investigation of short-range Al, Si order in synthetic anorthite by ^{29}Si MAS NMR spectroscopy. American Mineralogist, 77, 484–494.

Prévot, M., Hoffman, K.A., Goguitchaichvili, A., Doukhan, J.-C., Schcherbakov, V., and Bina, M. (2001) The mechanism of self-reversal of thermoremanence in natural hemoilmenite crystals: New experimental data and model. Physics of the Earth and Planetary Interiors, 126, 75–92.

Robinson, P., Harrison, R.J., McEnroe, S.A., and Hargraves, R.B. (2002) Lamellar magnetism in the haematite-ilmenite series as an explanation for strong remanent magnetization. Nature, 418, 517–520.

——— (2004) Nature and origin of lamellar magnetism in the hematite-ilmenite series. American Mineralogist, 89, 725–747.

Robinson, P., Harrison, R.J., and McEnroe, S.A. (2006a) Fe^{2+}/Fe^{3+} charge ordering in contact layers of lamellar magnetism: bond valence arguments. American Mineralogist, 91, 67–72.

Robinson, P., Heidelbach, F., Hirt, A.M., McEnroe, S.A., and Brown, LL. (2006b) Crystallographic-magnetic correlations in single crystal hemo-ilmenite: New evidence for lamellar magnetism. Geophysical Journal International, 165, 17–31.

Samuelsen, E.J. (1969) Spin waves in antiferromagnets with corrundum structure. Physica, 43, 353–374.

Samuelsen, E.J. and Shirane, G. (1970) Inelastic neutron scattering investigation of spin waves and magnetic interactions in α-Fe_2O_3. Physica Status Solidi, 42, 241–256.

van der Woude, F. (1966) Mössbauer effect in α-FeOOH. Physica Status Solidi, 17, 417–432.

Vinograd, V.L., Sluiter, M.H.F., Winkler, B., Putnis, A., Haêlenius, U., Galeand, J.D., and Becker, U. (2004) Thermodynamics of mixing and ordering in pyrope–grossular solid solution. Mineralogical Magazine, 68, 101–121.

Warren, M.C., Dove, M.T., and Redfern, S.A.T. (2000a) Ab initio simulations of cation ordering in oxides: application to spinel. Journal of Physics: Condensed Matter, 12, L43–48.

——— (2000b) Disordering of $MgAl_2O_4$ spinel from first principles. Mineralogical Magazine, 64, 311–317.

MANUSCRIPT RECEIVED JUNE 15, 2005
MANUSCRIPT ACCEPTED FEBRUARY 10, 2006
MANUSCRIPT HANDLED BY DARBY DYAR